

# DRAFT

# CMS Paper

*The content of this note is intended for CMS internal use and distribution only*

2020/02/17

Archive Hash: 1a32fb4-D

Archive Date: 2020/02/17

## Measurement of differential $t\bar{t}$ production cross sections for high- $p_T$ top quarks in proton-proton collisions at $\sqrt{s} = 13 \text{ TeV}$

The CMS Collaboration

### Abstract

A measurement of the production cross section for high transverse momentum ( $p_T$ ) top quark pairs is reported. The data set was collected during 2016 with the CMS detector at the CERN LHC from proton-proton collisions at a center-of-mass energy of 13 TeV, and corresponds to an integrated luminosity of  $35.9 \text{ fb}^{-1}$ . The measurement uses events where either both top quark candidates decay hadronically and are reconstructed as large-radius jets with  $p_T > 400 \text{ GeV}$ , or where one top quark decays hadronically and is identified as a single large-radius jet with  $p_T > 400 \text{ GeV}$  and the other top quark decays leptonically to a b jet, an electron or a muon, and a neutrino. The cross section is extracted differentially as a function of kinematic variables of the top quark or the top quark pair system. The results are presented at the particle level, within a region of phase space close to that of the experimental acceptance, and at the parton level, and are compared to various theoretical models. The measured differential cross sections are significantly lower in both decay channels in the phase space of interest, compared to the theory predictions, while the normalized differential cross sections are consistent between data and theory.

This box is only visible in draft mode. Please make sure the values below make sense.

PDFAuthor:	Konstantinos Kousouris, Yorgos Tsipolitis, Louise Skinnari, Susan Dittmer
PDFTitle:	Measurement of differential $t\bar{t}$ production cross sections for high- $p_T$ top quarks in proton-proton collisions at $\sqrt{s} = 13 \text{ TeV}$
PDFSubject:	CMS
PDFKeywords:	CMS, physics, top, $t\bar{t}$ , jets, boosted

Please also verify that the abstract does not use any user defined symbols



## 1 Introduction

The top quark completes the third generation of quarks in the standard model (SM), and a precise knowledge of its properties is critical for the overall understanding of the theory. Measurements of the top quark-antiquark pair ( $t\bar{t}$ ) production cross section confront the predictions from quantum chromodynamics (QCD), while being sensitive to effects of physics beyond the SM. The  $t\bar{t}$  production process is also a dominant SM background to many direct searches for new physics phenomena and therefore its detailed characterization is essential for new discoveries.

The large  $t\bar{t}$  yield expected in proton-proton (pp) collisions at the CERN LHC enables measurements of the  $t\bar{t}$  production rate in a large phase space, and more importantly, differentially, as a function of the kinematic properties of the top quark and  $t\bar{t}$  system. Such measurements have been performed by the ATLAS [1–6] and CMS [7–16] Collaborations at 7, 8, and 13 TeV center-of-mass energies, assuming a resolved final state where the decay products of the  $t\bar{t}$  pair can be reconstructed individually. This approach is possible for top quark transverse momenta  $p_T$  up to approximately 500 GeV. At higher  $p_T$ , the top quark decay products are highly collimated ("boosted") and they can no longer be reconstructed separately. In order to explore the highly boosted phase space, hadronic top quark decays are reconstructed as large-radius ( $R$ ) jets. Previous efforts in this domain by the ATLAS [17, 18] and CMS [19] Collaborations confirm that it is feasible to perform precise differential measurements of high- $p_T$   $t\bar{t}$  production and have also shown interesting deviations from the theory predictions.

In this paper, a measurement of the differential boosted  $t\bar{t}$  production cross section in the hadronic and lepton+jets final states is presented, using pp collisions at  $\sqrt{s} = 13$  TeV recorded with the CMS detector during the 2016 LHC run and amounting to a total integrated luminosity of  $35.9 \text{ fb}^{-1}$ . In the hadronic decay channel, each W boson arising from the top quark decays into a pair of light quarks. As a result, the final state consists of at least six partons (more are possible due to initial- and final-state radiation), two of which are b quarks. Due to the high boost considered in this measurement ( $p_T > 400$  GeV), the top quarks are reconstructed unambiguously as large- $R$  jets and the final state consists of at least two such jets. In the lepton+jets channel, one top quark decays to a hadronically-decaying W boson and a b quark ( $t \rightarrow Wb \rightarrow q\bar{q}'b$ ) and is reconstructed as a single large- $R$  jet, while the second top quark decays to a W boson, which in turn decays to a charged lepton ( $\ell$ ), either an electron or a muon ( $e/\mu$ ), and a neutrino, together with a b quark ( $t \rightarrow Wb \rightarrow \ell\nu b$ ). The presented measurements are performed using a significantly larger data set compared to the previous CMS results and utilize improved reconstruction techniques, leading to reduced uncertainties, which permits a confrontation of the theoretical predictions in a wider phase space.

The paper is organized as follows: Section 2 describes the main features of the CMS detector and the triggering system. Section 3 gives the details of the Monte Carlo (MC) simulations. The object reconstruction and the event selection is outlined in Sections 4 and 5, respectively. In Section 6, the estimation of the background contributions is explained, followed by a discussion of the signal extraction in Section 7. The systematic uncertainties are discussed in Section 8. The unfolding procedure used to obtain the particle- and parton-level cross sections and the resulting measurements are presented in Section 9. Finally, Section 10 provides the summary of the paper.

## 44 2 The CMS detector

45 The central feature of the CMS apparatus is a superconducting solenoid of 6 m internal diameter, providing a magnetic field of 3.8 T. Within the solenoid volume are a silicon pixel and strip  
 46 tracker, a lead tungstate crystal electromagnetic calorimeter (ECAL), and a brass and scintilla-  
 47 tor hadron calorimeter (HCAL), each composed of a barrel and two endcap sections. Forward  
 48 calorimeters extend the pseudorapidity ( $\eta$ ) coverage provided by the barrel and endcap detec-  
 49 tors. Muons are detected in gas-ionization chambers embedded in the steel flux-return yoke  
 50 outside the solenoid. A more detailed description of the CMS detector, together with a def-  
 51 inition of the coordinate system used and the relevant kinematic variables, can be found in  
 52 Ref. [20].  
 53

54 Events of interest are selected using a two-tiered trigger system [21]. The first level (L1), com-  
 55 posed of custom hardware processors, uses information from the calorimeters and muon de-  
 56 tectors to select events at a rate of around 100 kHz within a time interval of less than 4  $\mu$ s. The  
 57 second level, known as the high-level trigger (HLT), consists of a farm of processors running a  
 58 version of the full event reconstruction software optimized for fast processing, and reduces the  
 59 event rate to around 1 kHz before data storage.

## 60 3 Simulated events

61 MC simulation is used to generate samples for the  $t\bar{t}$  signal and to model the kinematic distribu-  
 62 tions of some of the background processes. Samples of simulated  $t\bar{t}$  events have been generated  
 63 at next-to-leading order (NLO) in QCD using POWHEG (v2) [22–26], assuming a top quark mass  
 64 of  $m_t = 172.5 \text{ GeV}$ . Single top quark production in the  $t$  channel or in association with a W bo-  
 65 son are simulated at NLO with POWHEG [27]. The production of W or Z bosons in association  
 66 with jets (V+jets), as well as QCD multijet events, are simulated with MG5\_AMC@NLO [28]  
 67 at leading order (LO), with the MLM matching algorithm [29]. Samples of diboson (WW, WZ,  
 68 ZZ) events are simulated using PYTHIA (v8.212) [30, 31]. used MC's in the analysis

69 All simulated events are processed with PYTHIA for modeling of the parton showering, hadron-  
 70 ization, and underlying event (UE). The NNPDF 3.0 [32] parton distribution functions (PDFs)  
 71 are used throughout, and the CUETP8M1 UE tune [33] is used for all processes except for the  
 72  $t\bar{t}$  and single top quark processes, for which the tune CUETP8M2T4 [34] is used. The simula-  
 73 tion of the CMS detector response is based on GEANT4 [35]. Additional pp interactions in the  
 74 same or neighboring bunch crossings (pileup) are simulated with PYTHIA and overlaid with  
 75 generated events according to the pileup distribution measured in data.

76 The various simulated processes are normalized to the best known theoretical cross sections,  
 77 namely the  $t\bar{t}$ , V+jets, and single top quark samples are normalized to NNLO precision in  
 78 QCD [36–38].

79 The measured cross sections for the  $t\bar{t}$  process are compared to theoretical predictions provided  
 80 by the following MC models: POWHEG combined with PYTHIA for the parton showering as de-  
 81 scribed above, or combined with HERWIG++ [39] and the corresponding EE5C UE tune [40].  
 82 In addition, a comparison is performed with MC@NLO [28] using PYTHIA for the parton show-  
 83 ering. The measured differential cross sections are additionally compared to state-of-the-art  
 84 theory calculations at NNLO precision.

## 4 Object reconstruction

The global event reconstruction (also called particle-flow event reconstruction [41]) aims to reconstruct and identify each individual particle in an event, with an optimized combination of all subdetector information. In this process, the identification of the particle type (photon, electron, muon, charged hadron, neutral hadron) plays an important role in the determination of the particle direction and energy. Photons (e.g. coming from  $\pi^0$  decays or from electron bremsstrahlung) are identified as ECAL energy clusters not linked to the extrapolation of any charged particle trajectory to the ECAL. Electrons (e.g. coming from photon conversions in the tracker material, B hadron semileptonic decays, or from the decay of a vector boson) are identified as primary charged tracks linked potentially to many ECAL energy clusters, corresponding to the tracks' extrapolation to the ECAL, and to possible bremsstrahlung photons emitted along the way through the tracker material. Muons (e.g. from vector bosons or B hadron semileptonic decays) are identified as tracks in the central tracker consistent with either a track or several hits in the muon system, and associated with calorimeter deposits compatible with the muon hypothesis. Charged hadrons are identified as charged particle tracks neither identified as electrons, nor as muons. Finally, neutral hadrons are identified as HCAL energy clusters not linked to any charged hadron trajectory, or as a combined ECAL and HCAL energy excess with respect to the expected charged hadron energy deposit.

The energy of photons is obtained from the ECAL measurement. The energy of electrons is determined from a combination of the track momentum at the main interaction vertex, the corresponding ECAL cluster energy, and the energy sum of all bremsstrahlung photons attached to the track. The energy of muons is obtained from the corresponding track momentum. The energy of charged hadrons is determined from a combination of the track momentum and the corresponding ECAL and HCAL energies, corrected for zero-suppression effects and for the response function of the calorimeters to hadronic showers. Finally, the energy of neutral hadrons is obtained from the corresponding corrected ECAL and HCAL energies.

Leptons and charged hadrons are required to be compatible with originating from the primary interaction vertex. The reconstructed vertex with the largest value of summed physics object  $p_T^2$  is taken to be the primary pp interaction vertex. The physics objects are the jets, clustered using the jet finding algorithm described below, with the tracks assigned to the vertex as inputs, and the associated missing transverse momentum, taken as the negative vector sum of the  $p_T$  of those jets. Charged hadrons that are associated with a pileup vertex are classified as pileup candidates and are ignored in the subsequent object reconstruction. Electron and muon objects are first identified from corresponding electron or muon particle-flow candidates. Next, jet clustering is performed on all particle-flow candidates that are not classified as pileup candidates. The jet clustering does not exclude the electron and muon particle-flow candidates, even if these have already been assigned to electron/muon objects. A dedicated overlap removal is therefore applied at the analysis level to avoid double counting.

Electrons and muons must have  $p_T > 50$  (20) GeV and  $|\eta| < 2.1$  for the  $\ell$ +jets channel (for vetoing leptons in the hadronic channel). Leptons are also required to be isolated according to the "mini isolation" ( $I_{\text{mini}}$ ) algorithm, which requires the  $p_T$  sum of tracks in a cone around the electron or muon to be less than a given fraction of the lepton  $p_T$  ( $p_T^\ell$ ). The cone width varies with the lepton  $p_T$  as  $\Delta R = 10/p_T^\ell$  for  $p_T^\ell < 200$  GeV and  $\Delta R = 0.05$  for  $p_T^\ell > 200$  GeV. A cut value of  $I_{\text{mini}} < 0.1$  is used. The usage of the mini-isolation algorithm retains high isolation efficiency also for leptons from boosted top quark decays. A looser lepton selection is used to define additional veto leptons in the  $\ell$ +jets channel, requiring  $p_T > 50$  GeV and  $|\eta| < 2.1$  but no isolation requirement. Correction factors are applied to account for differences

132 between data and the simulation in the modeling of the lepton identification, isolation, and  
 133 trigger efficiencies, determined as a function of the electron/muon  $|\eta|$  and  $p_T$ .

134 For each event, hadronic jets are clustered from the particles reconstructed by the particle-flow  
 135 algorithm using the infrared and collinear safe anti- $k_T$  algorithm [42, 43]. Two different jet col-  
 136 lections are considered for the analysis to identify b and t jet candidates, respectively. Small- $R$   
 137 jets are clustered using a distance parameter of 0.4 (used in the  $\ell$ +jets channel) and large- $R$  jets  
 138 using a distance parameter of 0.8 (used in the  $\ell$ +jets and hadronic channels). The jet momen-  
 139 tum is determined as the vectorial sum of all particle momenta in the jet, and is found from  
 140 simulation to be on average within 5–10% of the true momentum over the whole  $p_T$  spectrum  
 141 and detector acceptance. Additional pp pileup interactions can contribute additional tracks  
 142 and calorimetric energy depositions to the jet momentum. To mitigate this effect, charged par-  
 143 ticles identified to be originating from pileup vertices are discarded and an offset correction is  
 144 applied to correct for remaining contributions.

145 Jet energy corrections are derived from simulation studies to bring the average measured re-  
 146 sponse of jets to that of particle-level jets. In situ measurements of the momentum balance  
 147 in dijet, photon+jet, Z+jet, and QCD multijet events are used to account for any residual dif-  
 148 ferences in the jet energy scale between data and simulation [44]. The jet energy resolution  
 149 amounts typically to 15% at 10 GeV, 8% at 100 GeV, and 4% at 1 TeV. Additional selection cri-  
 150 teria are applied to each jet to remove jets potentially dominated by anomalous contributions  
 151 from various subdetector components or reconstruction failures.

152 In order to identify jets originating from hadronic decays of top quarks (t tagging), we use the  
 153 N-subjettiness variables [45]  $\tau_3$ ,  $\tau_2$ , and  $\tau_1$  computed using the jet constituents according to

$$\tau_N = \frac{1}{\sum_k p_{T,k} R} \sum_k p_{T,k} \min\{\Delta R_{1,k}, \Delta R_{2,k}, \dots, \Delta R_{N,k}\}, \quad (1)$$

154 where  $N$  denotes the number of reconstructed candidate subjets and  $k$  runs over the constituent  
 155 particles in the jet. The variable  $\Delta R_{i,k} = \sqrt{(\Delta y_{i,k})^2 + (\Delta \phi_{i,k})^2}$  is the angular distance between  
 156 the candidate subjet  $i$  and the particle  $k$ . The variable  $R$  is the characteristic jet radius ( $R = 0.8$  in  
 157 our case). The centers of hard radiation are found by performing the exclusive  $k_T$  algorithm [46,  
 158 47] on the jet constituents before the application of any grooming techniques.

159 In addition, a grooming technique is applied to remove soft, wide-angle radiation from the  
 160 jet and to improve the mass resolution. The algorithm employed is the “modified mass drop  
 161 tagger” [48, 49], also known as the soft-drop (SD) algorithm [50], with angular exponent  $\beta = 0$ ,  
 162 soft cutoff threshold  $z_{\text{cut}} < 0.1$ , and characteristic radius  $R_0 = 0.8$  [50]. The subjets within the  
 163 large- $R$  jets are identified by a reclustering of their constituents with the Cambridge–Aachen  
 164 algorithm [51, 52] and by reversing the last step of the clustering history.

165 Small- $R$  jets and subjets of the large- $R$  jets are identified as b quark candidates (b tagged) using  
 166 the combined secondary vertex (CSV) algorithm [53]. Data-to-simulation correction factors are  
 167 used to match the b tagging efficiency observed in simulation to that measured in data. The  
 168 typical efficiency of the b tagging algorithm for small- $R$  jets (large- $R$  subjets) is 63% (58%) for  
 169 true b jets, while the misidentification probability for non-b jets is 1%. For the large- $R$  subjets,  
 170 the efficiency for tagging true b jets drops from 65% to 40% as the  $p_T$  increases from 20 GeV to  
 171 1 TeV.

172 The missing transverse momentum vector  $\vec{p}_T^{\text{miss}}$  is defined as the projection on the plane per-  
 173 pendicular to the beams of the negative vector sum of the momenta of all the particle-flow

174 candidates in an event. Its magnitude is referred to as  $p_T^{\text{miss}}$ .

## 175 5 Event selection

### 176 5.1 Trigger

177 Different triggers were employed for the collection of signal events in the hadronic and  $\ell$ +jets  
 178 channels according to each event topology. The trigger used in the hadronic channel required  
 179 the presence of a jet with  $p_T > 180 \text{ GeV}$  at L1. At the HLT, large- $R$  jets were reconstructed from  
 180 particle-flow candidates using the anti- $k_T$  algorithm with a distance parameter of 0.8. The mass  
 181 of the jets at the HLT, after removal of soft particles, was required to be greater than  $30 \text{ GeV}$ .  
 182 Selected events were required to contain at least two such jets with  $p_T > 280$  ( $200$ )  $\text{GeV}$  for the  
 183 leading (trailing) jet. Finally, at least one of these jets was required to be  $b$  tagged, using the  
 184 CSV algorithm suitably adjusted for the HLT, with an average identification efficiency of 90%  
 185 for  $b$  jets. The aforementioned trigger ran for the entire 2016 run, collecting an integrated lumi-  
 186 nosity of  $35.9 \text{ fb}^{-1}$ . A second trigger with identical kinematic requirements but without any  $b$   
 187 tagging requirement was employed and ran on average every 21 bunch crossings, collecting an  
 188 integrated luminosity of  $1.67 \text{ fb}^{-1}$ . The events collected with the latter trigger are used for the  
 189 selection of a control data sample for estimating the QCD multijet background in the hadronic  
 190 channel, as described later. For the  $\ell$ +jets channel, the data were selected using triggers re-  
 191 quiring a single lepton, either an electron with  $p_T > 45 \text{ GeV}$  or a muon with  $p_T > 40 \text{ GeV}$  and  
 192  $|\eta| < 2.1$ , with no isolation criteria applied, as well as two small- $R$  jets with  $p_T > 200$  and  
 193  $50 \text{ GeV}$ , respectively.

### 194 5.2 Hadronic channel

195 All events considered in the hadronic channel are required to fulfill a common baseline selec-  
 196 tion. This requires the presence of at least two large- $R$  jets in the event with  $p_T > 400 \text{ GeV}$   
 197 and soft-drop masses in the range  $50\text{--}300 \text{ GeV}$ . In addition, events with at least one lepton are  
 198 vetoed in order to suppress leptonic top quark decays.

199 In order to discriminate between events that originate from  $t\bar{t}$  decays and QCD multijet produc-  
 200 tion, jet substructure variables are utilized. These variables are sensitive to the type of the jet,  
 201 and in particular to whether it comes from a single-prong decay, like ordinary quark or gluon  
 202 jets, or from a three-prong decay, such as the  $t \rightarrow W b \rightarrow \bar{q} q' b$  decay that is of interest here. The  
 203  $\tau_{1,2,3}$  variables of the two leading- $p_T$  large- $R$  jets are combined with a neural network (NN) to  
 204 form a multivariate event discriminant that characterizes each event, with values close to zero  
 205 indicating QCD dijet production and values close to one suggesting  $t\bar{t}$  production. The vari-  
 206 ables have been chosen such that the correlation with the number of  $b$ -tagged subjets, which is  
 207 used to define control regions for the QCD multijet background, is minimal. The NN consists  
 208 of two hidden layers with 16 and 4 nodes, respectively, and is implemented using the TMVA  
 209 toolkit [54]. More complex architectures have not improved the discriminating capabilities of  
 210 the NN. The training of the NN was performed with simulated QCD multijet (background) and  
 211  $t\bar{t}$  (signal) events that satisfy the baseline selection, using the back-propagation method and a  
 212 sigmoid activation function for the nodes. Excellent agreement between data and simulation  
 213 has been observed for the input variables in the phase space of the training.

214 On top of the baseline selection, sub-selection regions that serve different analysis purposes  
 215 are defined based on the NN output, the soft-drop mass of the jets, and the number of  $b$ -  
 216 tagged subjets in each large- $R$  jet. The signal region (SR), used to perform the differential  
 217 measurements, contains events collected with the signal trigger where both large- $R$  jets have

218 a b-tagged subjet and their masses lie in the range 120–220 GeV, while the NN output value  
 219 is greater than 0.8. This value has been chosen such that the tt signal over background ratio  
 220 is large, while keeping enough signal events with top quark  $p_T$  above 1 TeV. In this region,  
 221 more than 95% of the selected tt events originate from hadronic top quark decays. The QCD  
 222 multijet control region (CR) contains events collected with the control trigger that satisfy the  
 223 same requirements as the SR but with the b tagging requirement inverted (the large- $R$  jets  
 224 should not contain a b-tagged subjet). Additionally, expanded regions that include SR and CR  
 225 are defined for estimates of the background distributions. The signal region A ( $SR_A$ ) is the same  
 226 as SR with an extended requirement on the mass of the large- $R$  jets (50–300 GeV), while the  
 227 corresponding control region ( $CR_A$ ) has the b tagging condition reverted. It should be noted  
 228 that the events selected in  $SR_A$  and  $CR_A$  were collected with the signal and control triggers,  
 229 respectively. Finally, the signal region B ( $SR_B$ ) is used to constrain some of the signal modeling  
 230 uncertainties and has the same selection criteria as the SR but without any NN requirement.

### 231 5.3 Lepton+jets channel

232 The  $\ell + \text{jets}$  final state is identified through the presence of an electron or a muon, a small- $R$  jet  
 233 assumed to be produced by the decay of the b quark from the leptonic top quark decay, and a  
 234 large- $R$  jet corresponding to the hadronically decaying top quark. Small- $R$  jets are required to  
 235 have  $p_T > 50$  GeV and  $|\eta| < 2.4$ , while large- $R$  jets must fulfill  $p_T > 400$  GeV and  $|\eta| < 2.4$ .

236 All events are required to fulfill a set of preselection criteria, defined as follows:

- 237 • Exactly one signal electron or signal muon
- 238 • Zero additional veto leptons
- 239 • At least one leptonic-side jet (small- $R$  jet in the same hemisphere as the signal lepton,  
 240  $0.3 < |\Delta R(\ell, \text{jet})| < \pi/2$ ) b-jet probably in the “same” direction as the lepton
- 241 • At least one hadronic-side jet (large- $R$  jet in the opposite hemisphere to the signal  
 242 lepton,  $|\Delta R(\ell, \text{jet})| > \pi/2$ ) top jet candidate must be on the opposite direction from lepton
- 243 •  $p_T^{\text{miss}} > 50$  (35) GeV for the electron (muon) channel
- 244 • For events in the electron channel, a ‘triangular’ cut is required to ensure that the  
 245 missing transverse momentum vector does not point along the transverse direction  
 246 of the electron or the leading jet:  $|\Delta\phi(X, p_T^{\text{miss}})| < 1.5 \cdot \frac{p_T^{\text{miss}}}{7 \text{GeV}}$ , where X stands for  
 247 electron or leading small- $R$  jet

248 The more stringent  $p_T^{\text{miss}}$  and triangular criteria used in the electron channel are applied to  
 249 further reduce background from QCD multijet production.

250 Events that fulfill the preselection criteria are categorized according to whether the b (t) jet  
 251 candidate passes or fails the b (t) tagging criteria. The b(t) jet candidate is the highest- $p_T$   
 252 leptonic-side (hadronic-side) jet in the event. The N-subjettiness ratio  $\tau_3/\tau_2$  (abbreviated as  
 253  $\tau_{32}$ ) is used as the sensitive variable to distinguish a three-prong hadronic top quark decay  
 254 from background processes, requiring  $\tau_{32} < 0.81$ . A data-to-simulation efficiency correction  
 255 factor is extracted simultaneously with the integrated signal yield, as described in Section 7, to  
 256 correct the t tagging efficiency in simulation to match that in data. Events are divided into the  
 257 following categories:

- 258 • 0 t tag (0t): the t jet candidate fails the t tagging requirement
- 259 • 1 t tag, 0 b tag (1t0b): the t jet candidate passes the t tagging requirement, but the b  
 260 jet candidate fails the b tagging requirement

- 261 • 1 t tag, 1 b tag (1t1b): both the t jet candidate and the b jet candidate pass their  
 262 respective tagging requirement

263 These event categories are designed to have different admixtures of signal and background,  
 264 with the 0t region being the most background dominated and the 1t1b region the most signal  
 265 dominated.

## 266 6 Background estimation

267 The dominant background in the hadronic channel is QCD multijet production, while in the  
 268 ℓ+jets channel, the dominant sources of background events include non-signal tt, single top  
 269 quark, W+jets, and QCD multijet production. Non-signal tt production comprises dileptonic  
 270 and hadronic final states, in addition to τ+jets events where the tau lepton does not decay to  
 271 an electron or a muon.

272 In the hadronic channel, the background due to QCD multijet production is significantly suppressed  
 273 through a combination of subjet b tagging requirements and the event NN output. The remaining contribution is estimated from a control data sample. The two elements that are  
 274 determined from data are the distribution  $Q(x)$  of the QCD multijet background as a function  
 275 of an observable of interest  $x$ , and the absolute normalization  $N_{\text{QCD}}$ . The QCD template  $Q(x)$   
 276 is taken from the data control region CR<sub>A</sub>. The tt signal contamination of this control sample,  
 277 based on the simulation, is of the order of 1%. The normalization of the QCD multijet back-  
 278 ground ( $N_{\text{QCD}}$ ) is determined from a maximum likelihood fit to the data in SR<sub>A</sub> of the soft-drop  
 279 mass of the t jet candidate,  $m^t$ , where the t jet candidate is taken as the leading- $p_T$  large- $R$  jet.  
 280 The fit is described by the equation

$$281 D(m^t) = N_{\text{tt}} T(m^t; k_{\text{scale}}, k_{\text{res}}) + N_{\text{QCD}}(1 + k_{\text{slope}} m^t) Q(m^t) + N_{\text{bkg}} B(m^t), \quad (2)$$

282 which contains the distributions  $T(m^t)$  and  $B(m^t)$  of the signal and the subdominant back-  
 283 grounds, respectively, taken from the simulation, and the distribution  $Q(m^t)$  of the QCD mul-  
 284 tijet background, taken from the control sample in data. To account for a possible difference in  
 285 the QCD multijet  $m^t$  distribution between the control and signal regions, a linear modification  
 286 factor  $(1 + k_{\text{slope}} m^t)$  is introduced, inspired by the simulation, but with the slope parameter  
 287  $k_{\text{slope}}$  left free in the fit. Also free in the fit are the normalization factors  $N_{\text{tt}}$ ,  $N_{\text{QCD}}$ , and  $N_{\text{bkg}}$ .  
 288 Two additional nuisance parameters are introduced in the simulated tt distribution,  $k_{\text{scale}}$  and  
 289  $k_{\text{res}}$ , which account for possible differences between data and simulation in the scale and reso-  
 290 lution of the  $m^t$  parameter. The fit is performed with the ROOFIT toolkit [55] and the fit results  
 291 are shown in Fig. 1 and Table 1. The fitted tt yield is significantly lower than the expectation  
 292 (9885), which implies that the fiducial cross section is lower compared to the POWHEG+PYTHIA  
 293 prediction with a post-fit signal strength of  $0.64 \pm 0.03$ . This value is used to scale down the  
 294 expected tt signal yields from the POWHEG+PYTHIA simulation in the various signal regions  
 295 in the subsequent figures with data vs simulation comparisons. The nuisance parameters that  
 296 control the scale and the resolution of the reconstructed mass are consistent with one, confirm-  
 297 ing the excellent agreement between data and simulation of this variable.

298 The subdominant background processes, namely single top quark production and vector bosons  
 299 produced in association with jets, have a negligible contribution in the signal region (below 1%  
 300 in the entire phase space) and are fixed to the predictions from simulation.

301 Figure 2 shows the distribution of the NN output in SR<sub>B</sub> and Figs. 3, 4 show the kinematic  
 302 properties of the two top quark candidates and the tt system, respectively. Also, the soft-drop

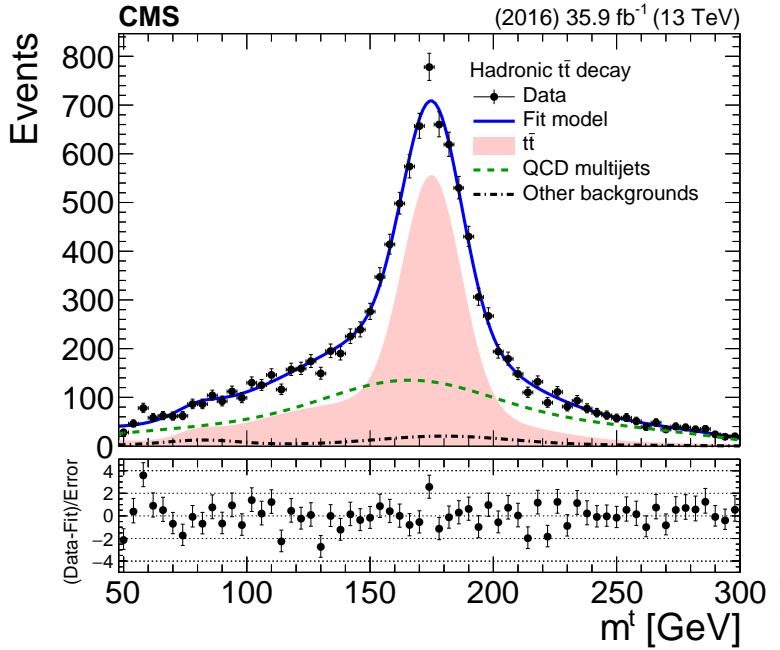


Figure 1: Result of the fit to data of the soft-drop mass of the  $t$  jet candidate,  $m^t$ , in  $\text{SR}_A$  for the hadronic channel. The shaded area shows the  $t\bar{t}$  contribution, the dashed line shows the QCD multijet background, and the double-dashed line shows the other subdominant backgrounds. The solid line shows the combined signal plus background fit model, and the data points are shown with solid markers. The bottom panel shows the data minus the fit model, divided by the fit uncertainty.

Table 1: Post-fit values of the nuisance parameters for the fit to data in  $\text{SR}_A$  in the hadronic channel.

Parameter	Value
$k_{\text{res}}$	$0.960 \pm 0.026$
$k_{\text{scale}}$	$1.002 \pm 0.002$
$k_{\text{slope}}$	$(5.7 \pm 1.4) \times 10^{-3}$
$N_{\text{bkg}}$	$400 \pm 255$
$N_{\text{QCD}}$	$4539 \pm 247$
$N_{t\bar{t}}$	$6238 \pm 181$

303 masses of the two jets are shown in Fig. 5. In these figures, the  $t\bar{t}$  and QCD multijet processes  
 304 are normalized according to the results of the fit in  $\text{SR}_A$  described above, while the yields of the  
 305 subdominant backgrounds are taken from the simulation. Table 2 summarizes the event yields  
 306 in the SR.

Table 2: Observed and predicted event yields with their respective statistical uncertainty in the signal region for the hadronic channel. The  $t\bar{t}$  and QCD multijet yields are obtained after the fit in SR<sub>A</sub>.

Process	Number of events
$t\bar{t}$	$4244 \pm 127$
QCD multijets	$1876 \pm 102$
Single t	$83 \pm 41$
$W + \text{jets}$	$58 \pm 29$
$Z + \text{jets}$	$12 \pm 6$
Total	$6273 \pm 171$
Data	6274

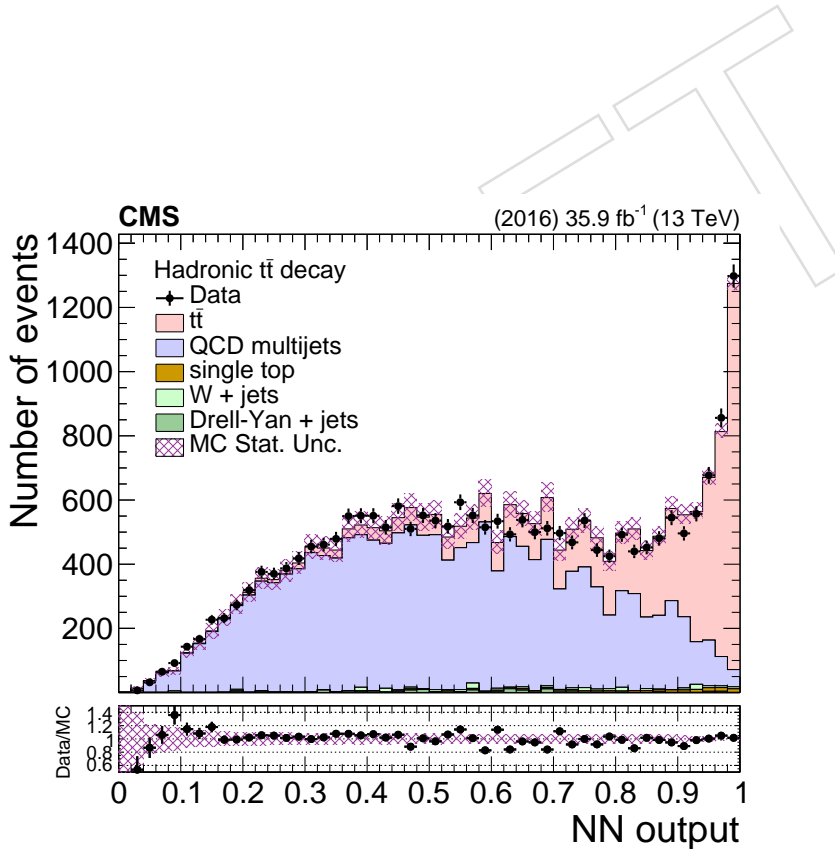


Figure 2: Comparison between data and simulation in SR<sub>B</sub> (same as the SR, without any NN requirement) of the NN output in the hadronic channel. The  $t\bar{t}$  and QCD multijet processes are normalized according to the post-fit values of the respective yields and are shown as stacked histograms. The data points are shown with solid markers, while the shaded band represents the statistical uncertainty in the simulation. The bottom panel shows the data divided by the sum of the prediction from the simulation.

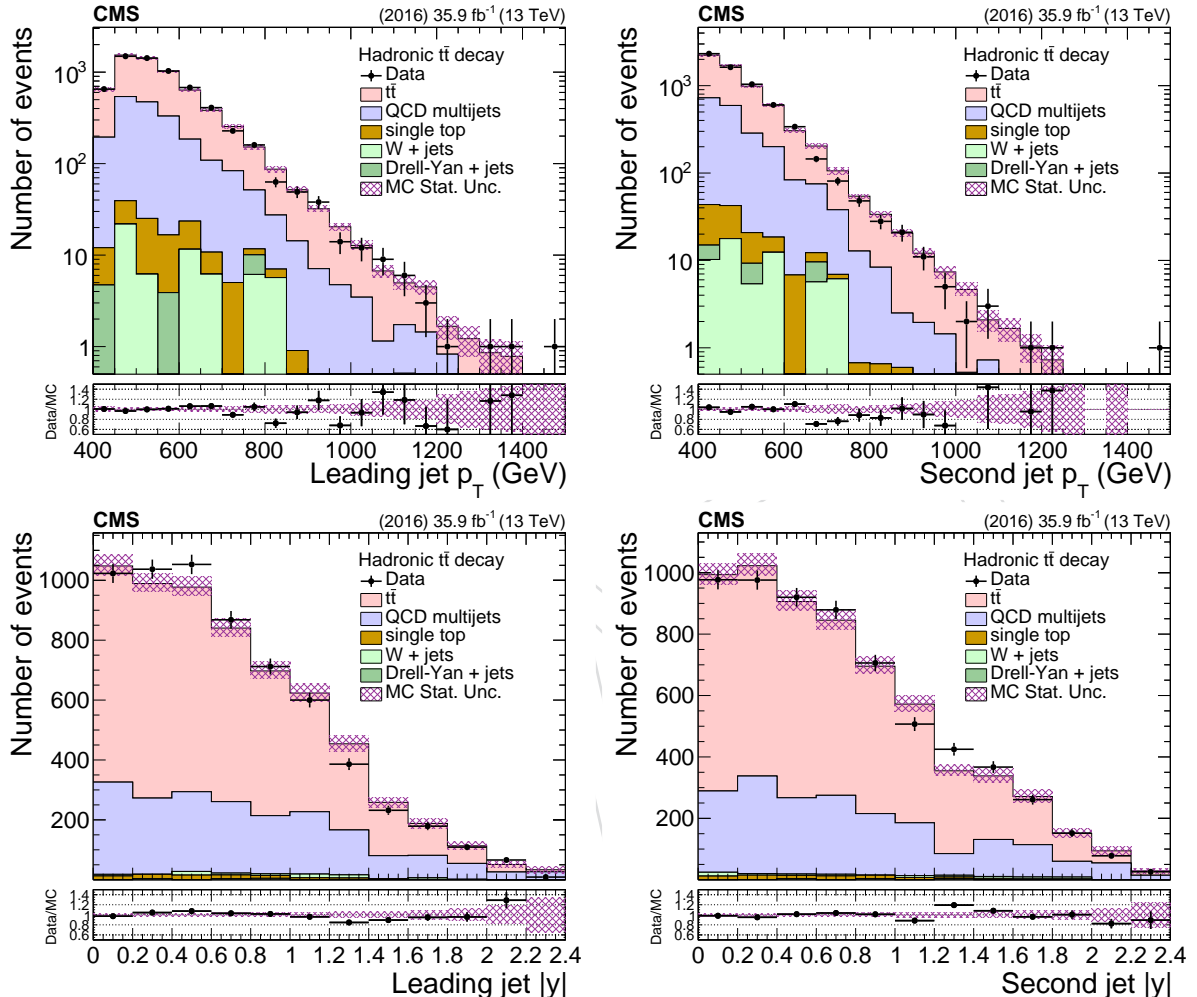


Figure 3: Comparison between data and simulation in the signal region of the  $p_T$  (top row) and absolute rapidity (bottom row) of the leading (left column) and subleading (right column) large- $R$  jets in the hadronic channel. The  $t\bar{t}$  and QCD multijet processes are normalized according to the post-fit values of the respective yields and are shown as stacked histograms. The data points are shown with solid markers, while the shaded band represents the statistical uncertainty in the simulation. The bottom panel shows the data divided by the sum of the prediction from the simulation.

by saying normalised according to the post-fit values  
we mean that we take the shape and then multiply it  
with the yield found in the fit?

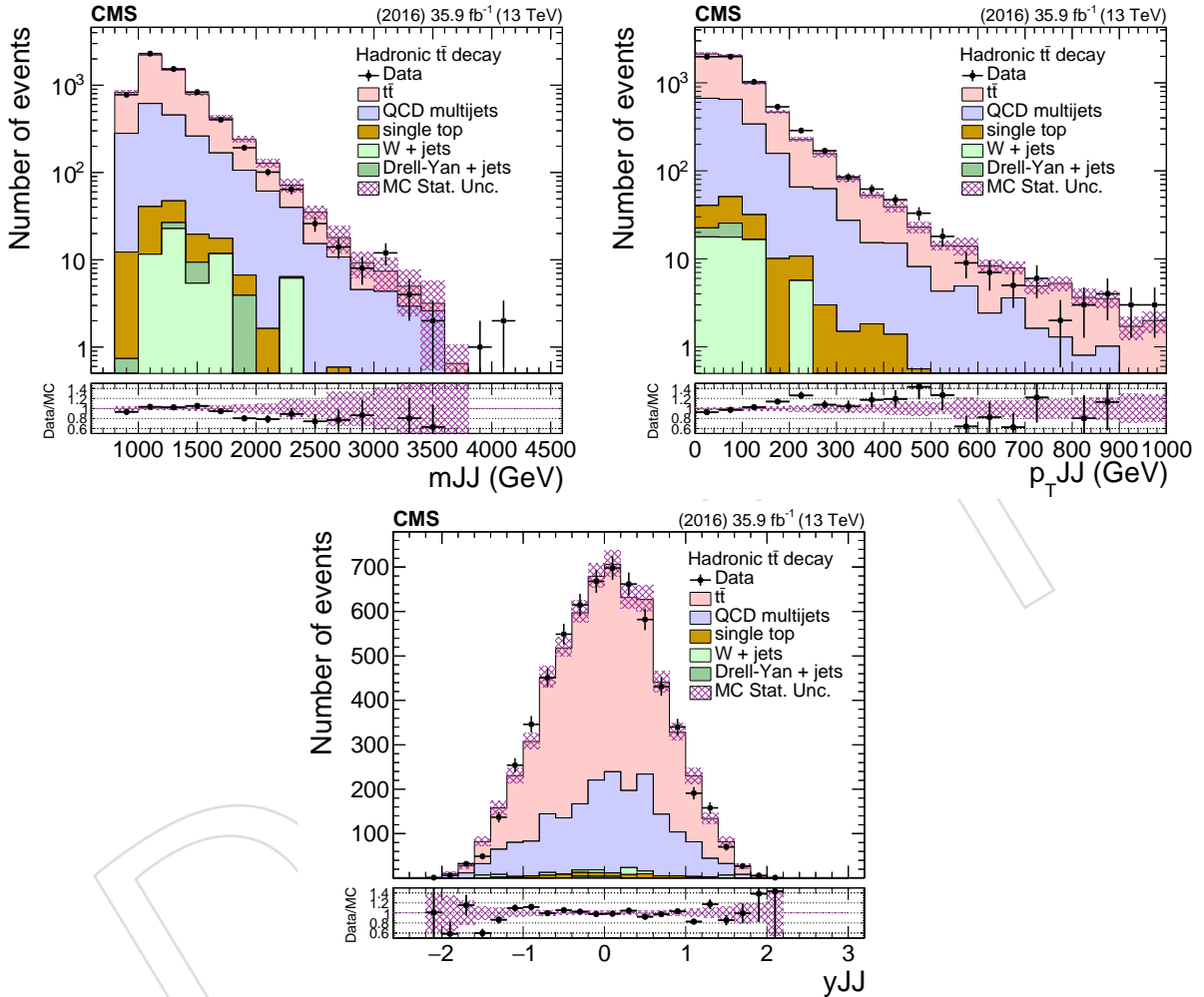


Figure 4: Comparison between data and simulation in the signal region in the hadronic channel of the  $t\bar{t}$  system variables reconstructed from the two leading large- $R$  jets, specifically, the invariant mass (top left),  $p_T$  (top right), and rapidity (bottom). The  $t\bar{t}$  and QCD multijet processes are normalized according to the post-fit values of the respective yields and are shown as stacked histograms. The data points are shown with solid markers, while the shaded band represents the statistical uncertainty in the simulation. The bottom panel shows the data divided by the sum of the prediction from the simulation.

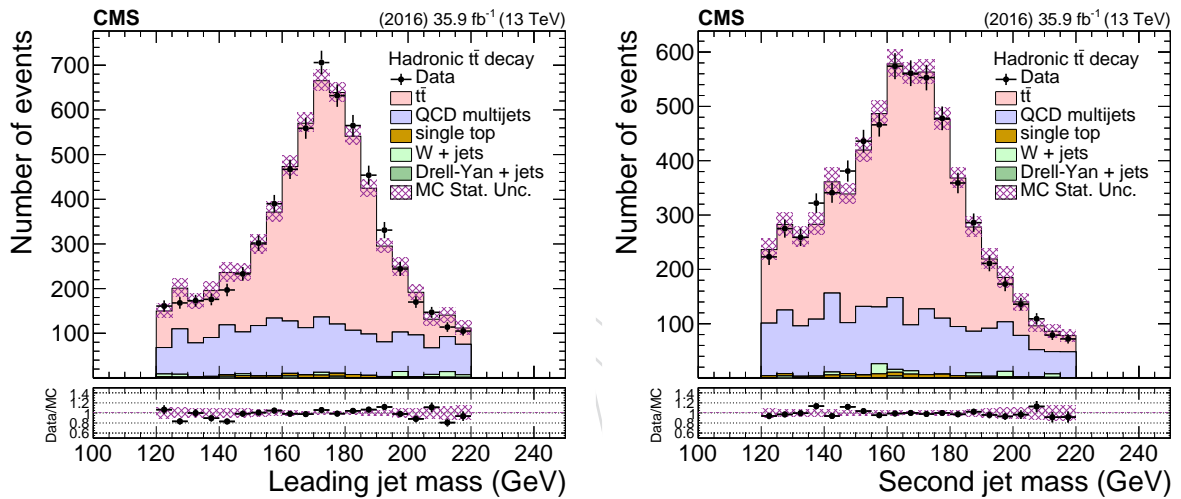


Figure 5: Comparison between data and simulation in the signal region of the mass of the leading (left) and subleading (right) large- $R$  jets in the hadronic channel. The  $t\bar{t}$  and QCD multijet processes are normalized according to the post-fit values of the respective yields and are shown as stacked histograms. The data points are shown with solid markers, while the shaded band represents the statistical uncertainty in the simulation. The bottom panel shows the data divided by the sum of the prediction from the simulation.

307 In the  $\ell$ +jets channel, background events due to non-signal  $t\bar{t}$ , single top quark,  $W/Z$ +jets, and  
 308 diboson production are estimated from simulation. The QCD multijet background is modeled  
 309 with data-based techniques, using a data sideband region that is defined by inverting the iso-  
 310 lation requirement on the lepton and relaxing the lepton identification criteria. The predicted  
 311 contributions to the sideband region from signal and other background events are subtracted  
 312 from the observed data distribution in the sideband region to yield the kinematic distributions  
 313 for QCD multijet events. The normalization of the QCD multijet background is extracted from  
 314 a maximum likelihood fit, described in Section 7.2; an initial estimate of its normalization is  
 315 taken as the simulated prediction in the signal region. The normalizations of the other back-  
 316 ground processes are also constrained through the fit.

## 317 7 Signal extraction

### 318 7.1 Hadronic channel

319 In the hadronic channel, the  $t\bar{t}$  signal is extracted from data by subtracting the contribution  
 320 from the background processes. The signal extraction is performed differentially, as a function  
 321 of seven variables:  $p_T$  and absolute rapidity  $|y|$  of the leading and subleading  $t$  jet, as well as  
 322 the mass,  $p_T$ , and  $y$  of the  $t\bar{t}$  system. That is:

$$S(x) = D(x) - R_{\text{yield}} N_{\text{QCD}} Q(x) - B(x), \quad (3)$$

323 where  $x = p_T^{t1,2}, |y^{t1,2}|, m^{t\bar{t}}, p_T^{\bar{t}}$ , or  $y^{\bar{t}}$ ,  $S(x)$  is the  $t\bar{t}$  signal,  $D(x)$  is the measured distribution in  
 324 data,  $Q(x)$  is the QCD multijet distribution, and  $B(x)$  is the contribution from the subdominant  
 325 backgrounds (for which both the distribution and the normalization are taken from the simula-  
 326 tion). These quantities are taken from the signal region. The variable  $N_{\text{QCD}}$  is the fitted number  
 327 of QCD multijet events in  $\text{SR}_A$  and the factor  $R_{\text{yield}}$  is found (in simulation) to be independent  
 328 of the  $b$  tagging requirement and therefore it is estimated from the QCD multijet control data  
 329 sample as  $R_{\text{yield}} = N_{\text{QCD}}^{\text{SR}} / N_{\text{QCD}}^{\text{SR}_A} = N_{\text{QCD}}^{\text{CR}} / N_{\text{QCD}}^{\text{CR}_A} \approx 0.38 \pm 0.02$ .

### 330 7.2 Lepton+jets channel

331 For the analysis in the  $\ell$ +jets channel, the  $t\bar{t}$  signal strength,  $t$  tagging efficiency scale factor, and  
 332 background normalizations are determined in a simultaneous binned maximum likelihood fit  
 333 to the data across the different analysis event categories.

334 The 0t, 1t0b, and 1t1b event categories are fitted simultaneously, normalizing each background  
 335 component to the same cross section in all categories. The fit result is expressed in terms of a  
 336 multiplicative factor, the signal strength  $\eta$ , applied to the input  $t\bar{t}$  cross section. Different vari-  
 337 ables are used to discriminate the  $t\bar{t}$  signal from the background processes. The small- $R$  jet  $\eta$   
 338 distribution is used in the 0t and 1t0b categories, while the large- $R$  jet soft-drop mass distribu-  
 339 tion is used in the 1t1b region. These distributions were chosen to have good discrimination  
 340 between  $t\bar{t}$ ,  $W$ +jets, and QCD multijet production, as  $t\bar{t}$  events tend to be produced more cen-  
 341 trally than the background and the soft-drop mass distribution peaks around the top quark  
 342 mass for signal events. The  $t\bar{t}$  signal and  $t\bar{t}$  background distributions are merged into a sin-  
 343 gle distribution for the purpose of the fit, essentially constraining the semileptonic branching  
 344 fraction to be equal to that provided by the simulation.

345 Background normalizations and experimental sources of systematic uncertainty are treated as  
 346 nuisance parameters in the fit. The uncertainties due to pileup reweighting, lepton scale fac-

tors, jet energy scale and resolution, b tagging efficiency, and t tagging efficiency are treated as  
 uncertainties in the shape of the input templates. Two separate nuisance parameters are used  
 to describe the t tagging uncertainty: one for the t tagging scale factor that is applied to the  $t\bar{t}$   
 and single top quark ( $tW$ ) samples, where we expect the t-tagged jet to correspond to a true top  
 quark decay, while the t mistag scale factor is applied for the remaining background samples.  
 The uncertainties in the luminosity and background normalizations are treated as rate uncer-  
 tainties. The event categories that are fitted are designed such that the t tagging efficiency is  
 constrained by the relative population of events in the three categories. The varying admix-  
 tures of signal and background between the different event categories allows constraining the  
 background normalizations. The measurement of the signal strength is correlated with the var-  
 ious nuisance parameters, with the strongest correlation being with the t tagging efficiency, as  
 expected. For the shape uncertainties, the nuisance parameter is used to interpolate between  
 the nominal kinematic distribution and distributions corresponding to  $\pm 1$  standard deviation  
 ( $\sigma$ ) variations in the given uncertainty. The uncertainties due to the theoretical modeling are  
 evaluated independently from the fit.

The  $e/\mu+jets$  channels are fitted simultaneously, with most nuisance parameters constrained to  
 be the same in both channels. The nuisance parameters associated with the electron and muon  
 scale factors are treated separately, as are the electron and muon QCD multijet background  
 normalizations. The posterior kinematic distributions for the three event categories are shown  
 in Fig. 6. The event counts that account for all posterior parameters are given in Table 3.

Process	Number of events ( $\mu+jets$ channel)		
	0t	1t0b	1t1b
$t\bar{t}$	$16772 \pm 1438$	$4245 \pm 174$	$3905 \pm 80$
Single t	$3286 \pm 587$	$282 \pm 68$	$153 \pm 34$
$W+jets$	$23104 \pm 2871$	$2368 \pm 318$	$105 \pm 20$
$Z+jets$	$2582 \pm 680$	$234 \pm 69$	$19 \pm 10$
Diboson	$557 \pm 155$	$31 \pm 10$	$2 \pm 1$
QCD multijets	$2833 \pm 1207$	$159 \pm 76$	$43 \pm 22$
Total	$49135 \pm 3549$	$7320 \pm 383$	$4228 \pm 93$
Data	49137	7348	4187

Process	Number of events ( $e+jets$ channel)		
	0t	1t0b	1t1b
$t\bar{t}$	$10707 \pm 938$	$2835 \pm 116$	$2670 \pm 66$
Single t	$2267 \pm 403$	$191 \pm 47$	$107 \pm 24$
$W+jets$	$13945 \pm 1742$	$1445 \pm 194$	$62 \pm 12$
$Z+jets$	$1068 \pm 295$	$118 \pm 37$	$17 \pm 15$
Diboson	$373 \pm 105$	$22 \pm 7$	$2 \pm 1$
QCD multijets	$3200 \pm 735$	$242 \pm 80$	$31 \pm 30$
Total	$31560 \pm 2171$	$4854 \pm 247$	$2889 \pm 79$
Data	31559	4801	2953

Table 3: Posterior signal and background event yields in the 0t, 1t0b, and 1t1b categories, together with the observation in data. The uncertainties include all posterior experimental uncertainties.

Figure 7 shows the  $p_T$  and  $y$  distributions for the t jet candidate in each of the three event cat-  
 egories for the combined  $\ell+jets$  channel. These distributions use the posterior t tagging scale

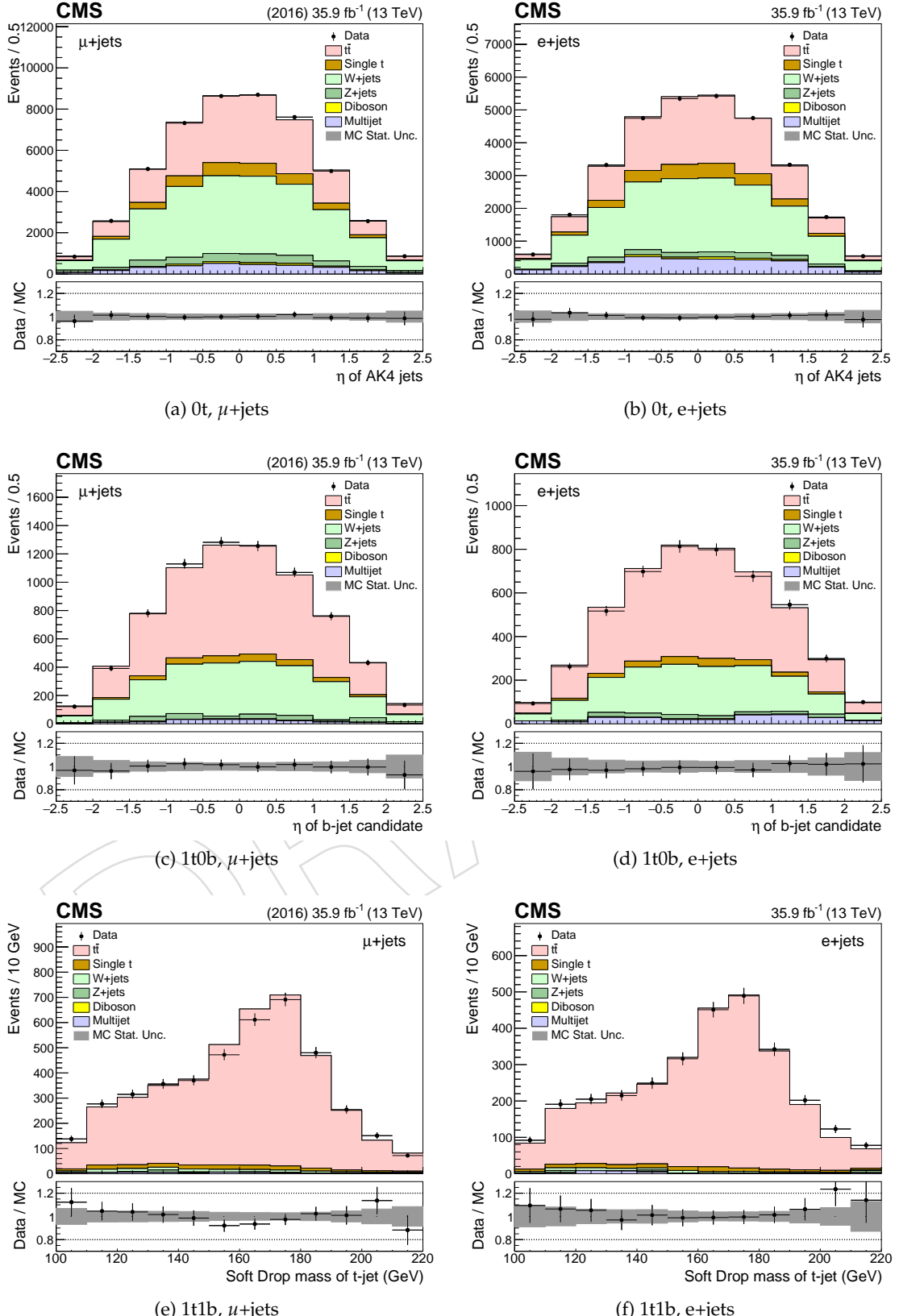


Figure 6: Posterior kinematic distributions for the maximum likelihood fit. Different event categories and variables are used:  $\eta$  distribution for the small- $R$  jet in 0t events (top),  $\eta$  distribution of the b jet candidate in 1t0b events (middle), and soft drop mass of the t jet candidate in 1t1b events (bottom), in the  $\mu$ +jets (left) and e+jets (right) channel. The data points are shown with solid markers, while the signal and background predictions are shown as stacked histograms. The bottom panel shows the data divided by the sum of the prediction from the simulation (solid markers) and the systematic uncertainty from the fit (shaded band).

369 factor and background normalizations, but not the posterior values of other nuisance parameters. The posterior t tagging efficiency (misidentification) scale factor is  $1.04 \pm 0.06$  ( $0.79 \pm 0.06$ ),  
 370 with an additional t jet  $p_T$  and  $\eta$  dependent uncertainty in the range 1–8% (1–13%). The post-fit  
 371 background normalizations are generally in good agreement with their corresponding pre-fit  
 372 values, only the W+light jet normalization is low by about  $1\sigma$ .  
 373

374 The posterior signal strength as determined in the fit is  $0.81 \pm 0.05$ , i.e. the  $t\bar{t}$  simulation is  
 375 observed to overestimate the data by roughly 25% in the fiducial phase space region. Although  
 376 the measured signal strength extrapolated from the fit is not directly used in measuring the dif-  
 377 ferential cross section, it serves as an indicator of the level of agreement between the measured  
 378 integrated  $t\bar{t}$  cross section and the prediction from the simulation in the boosted regime.

## 379 8 Systematic uncertainties

380 The systematic uncertainties considered in this measurement originate from both experimental  
 381 and theoretical sources. The former include all uncertainties related to the differences in the  
 382 particle reconstruction and identification performance between data and simulation, as well as  
 383 the background modeling. The latter are related to the  $t\bar{t}$  signal simulation and affect primar-  
 384 ily the unfolded results through the acceptance, efficiency, and migration matrices. For each  
 385 systematic variation, the differential cross section measurement is repeated and the difference  
 386 with respect to the nominal result is taken as the effect of this variation on the measurement.

387 A number of experimental uncertainties affect the measurement. The dominant sources of  
 388 systematic uncertainty in the hadronic channel are due to the jet energy scale and the subjet  
 389 b tagging efficiency. In the  $\ell+jets$  channel, the t tagging and b tagging efficiency uncertainties  
 390 result in the largest contributions. The different sources are described in detail in the list below:

- 391 • ***QCD multijet background (hadronic)***: The fitted QCD multijet yield uncertainty is used,  
 392 as well as the uncertainty in  $R_{yield}$  (Eq. 3). The impact of the shape uncertainties,  
 393 estimated by comparing the distribution of each variable between the signal region  
 394 SR and the control region CR (see Section 5) in simulated events, as well as the  
 395 different pileup profiles for data collected with the control trigger compared to the  
 396 signal trigger, are of the order of 1%. The uncertainty in  $R_{yield}$  is dominated by the  
 397 uncertainty of the method (estimated with simulated events), while there is a smaller  
 398 statistical contribution.
- 399 • ***Subdominant backgrounds (hadronic)***: The expected yield of the subdominant back-  
 400 ground processes estimated from the simulation (single top quark production and  
 401 vector bosons produced in association with jets) is varied by  $\pm 50\%$ , leading to a  
 402 negligible uncertainty (smaller than 1%).
- 403 • ***Background estimate ( $\ell+jets$ )***: An a priori uncertainty of 30% is applied to the sin-  
 404 gle top quark and W+jets background normalizations. An additional uncertainty in  
 405 the flavor composition of the W+jets process is considered, allowing the light- and  
 406 heavy-flavor components to vary independently with a 30% normalization uncer-  
 407 tainty. For the QCD multijet normalization, an a priori uncertainty of 50% is used  
 408 to reflect the combined uncertainty in the normalization and the extraction of the  
 409 kinematic distributions from the data sideband region. These are all constrained in  
 410 the maximum likelihood fit.
- 411 • ***Jet energy scale***: The uncertainty in the energy scale of each reconstructed large- $R$   
 412 jet, referred to as the jet energy scale (JES) uncertainty, is a leading experimental  
 413 uncertainty in the hadronic channel. It is divided in 24 independent sources [44]

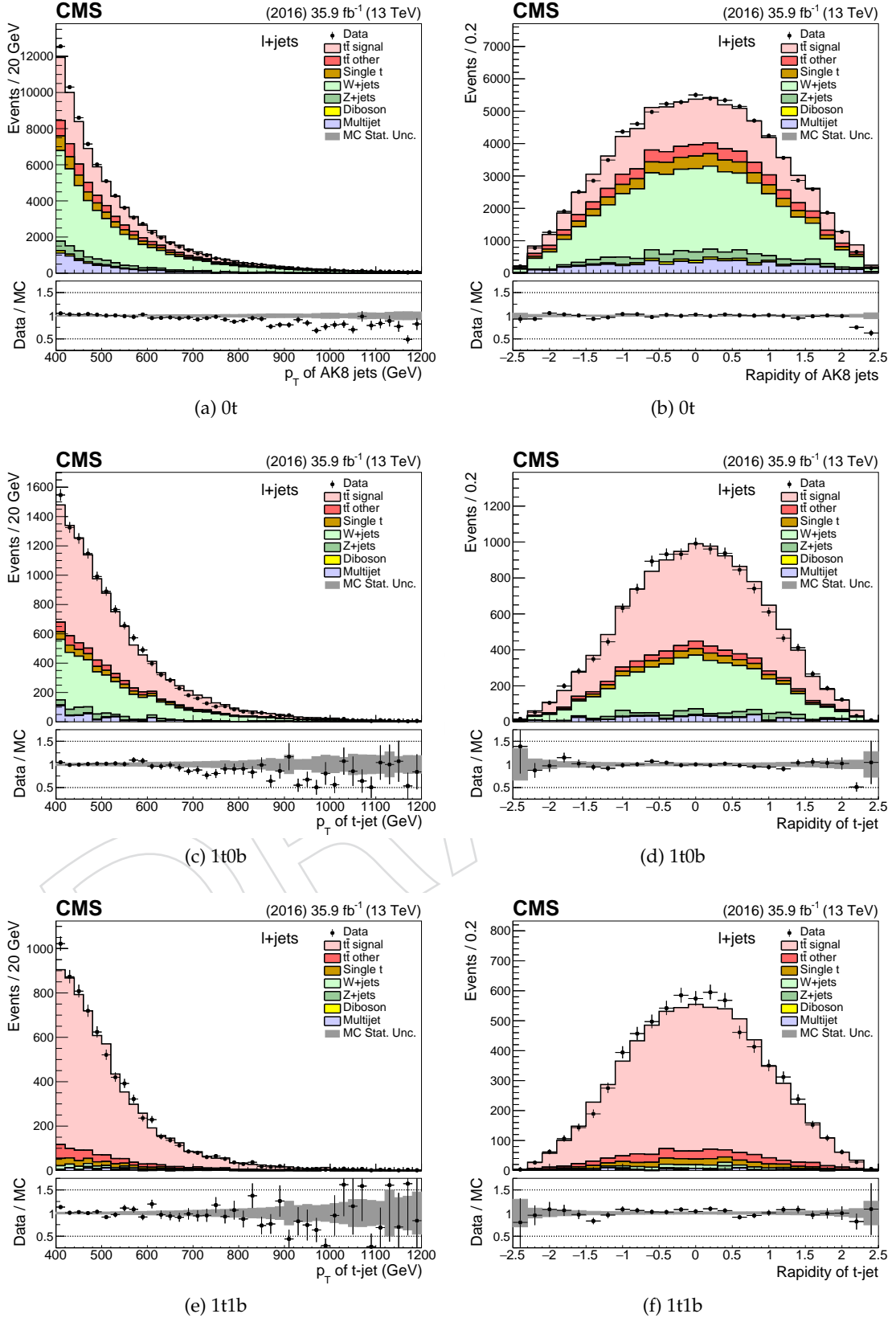


Figure 7: Distributions of the  $p_T$  (left) and  $y$  (right) of the t jet candidate for the 0t (top), 1t0b (middle), and 1t1b (bottom) regions for events in the combined  $\ell$ +jets channel. The posterior t tag scale factor and background normalizations are used. The data points are shown with solid markers, while the signal and background predictions are shown as stacked histograms. The bottom panel shows the data divided by the sum of the prediction from the simulation (solid markers) and the systematic uncertainty from the fit (shaded band).

414 and treated as follows: for each variation a new jet collection is created and the event  
 415 interpretation is repeated. This results not only in variations of the  $p_T$  scale itself, but  
 416 may also lead to different t jet candidates. The  $p_T$  and  $\eta$  dependent JES uncertainty is  
 417 of the order of 1–2% per jet. The resulting uncertainty in the measured cross section  
 418 is typically of the order of 10% but it can be much larger at high top quark  $p_T$ . For  
 419 the  $\ell$ +jets channel, the jet energy scale uncertainty is estimated for both small- $R$  and  
 420 large- $R$  jets by shifting the jet energy in simulation up or down by their  $p_T$  and  $\eta$   
 421 dependent uncertainties, with a resulting impact on the differential cross section  
 422 measurements of 1–10%.

- 423 • **Jet energy resolution:** The impact on the measurement due to the jet energy resolution  
 424 (JER) is determined by smearing the jets according to the JER uncertainty [44]. The  
 425 effect on the cross section is relatively small, at the level of 2%.
- 426 • **t tagging efficiency ( $\ell$ +jets):** The t tagging efficiency and its associated uncertainty is  
 427 simultaneously extracted with the signal strength and background normalizations  
 428 in the likelihood fit for the  $\ell$ +jets analysis, described in Section 7. The uncertainty in  
 429 the t tagging efficiency is in the range 6–10%, while for the misidentification rate it  
 430 is 8–15%, depending on t jet  $p_T$  and  $\eta$ .
- 431 • **Subjet b tagging efficiency (hadronic):** The uncertainty in the identification of b subjets  
 432 within the large- $R$  jets (estimated in [53]) is a leading experimental uncertainty in the  
 433 hadronic channel. The effect on the cross sections is of the order of 10%, relatively  
 434 flat in all the observables. Unlike the uncertainty associated with the JES, the b-subjet  
 435 tagging uncertainty therefore largely cancels in the normalized cross sections.
- 436 • **b tagging efficiency ( $\ell$ +jets):** For the  $\ell$ +jets channel, the small- $R$  jet b tagging effi-  
 437 ciency in the simulation is corrected to match that measured in data using  $p_T$ - and  
 438  $\eta$ -dependent scale factors [53]. The resulting uncertainty in the differential cross  
 439 sections is about 1–2%. The b tagging efficiency and light jet misidentification un-  
 440 certainties are treated as fully correlated.
- 441 • **Pileup:** The uncertainty related to the modeling of additional pileup interactions is a  
 442 subdominant uncertainty. The impact on the measurement is estimated by varying  
 443 the total inelastic cross section used to weight the simulated events by  $\pm 4.6\%$  [56].  
 444 The effect on the cross sections is negligible (below 1%).
- 445 • **Trigger (hadronic):** The uncertainty associated with the trigger, accounting for the  
 446 difference between the simulated and observed trigger efficiency, is well below 1%  
 447 in the phase space of the hadronic channel.
- 448 • **Lepton identification and trigger ( $\ell$ +jets):** The performance of the lepton identification,  
 449 reconstruction, trigger, and isolation constitutes a small source of systematic un-  
 450 certainty. Correction factors used to modify the simulation to match the efficiencies  
 451 observed in data are estimated with a tag-and-probe method using  $Z \rightarrow \ell\ell$  decays.  
 452 The corresponding uncertainty is determined by varying the correction factors up  
 453 or down within their uncertainties. The resulting systematic uncertainties depend  
 454 on lepton  $p_T$  and  $\eta$ , and are in the range 1–7% and 1–5% for electrons and muons,  
 455 respectively.
- 456 • **Luminosity:** The uncertainty in the measurement of the integrated luminosity is  
 457 2.5% [57].
- 458 The **theoretical** uncertainties are divided into **two sub-categories**: sources of systematic un-  
 459 certainty related to the matrix element of the hard scatter process and sources related to the  
 460 modeling of the parton shower and the underlying event. The first category (consisting of the

461 first three sources below) is evaluated using variations of the simulated event weights, while  
 462 the second category is evaluated with dedicated, alternative MC samples with modified pa-  
 463 rameters. These sources are:

- 464 • **Parton distribution functions:** The uncertainty due to PDFs is estimated by applying  
 465 event weights corresponding to the 100 replicas of the NNPDF set [32]. For each  
 466 observable we compute its standard deviation from the 100 variations.
- 467 • **Renormalization and factorization scales:** This source of systematic uncertainty is esti-  
 468 mated by applying event weights corresponding to different factorization and renor-  
 469 malization scale options. Both scales are varied independently by a factor of two up  
 470 or down in the event generation, omitting the two cases where the scales are varied  
 471 in opposite directions, and taking the envelope of the six resulting variations.
- 472 • **Strong coupling constant ( $\alpha_S$ ):** The uncertainty associated with the  $\alpha_S$  is estimated by  
 473 applying event weights corresponding to higher or lower values of  $\alpha_S$  for the matrix  
 474 element using the variations of the NNPDF set [32].
- 475 • **Initial- and final-state radiation:** The uncertainty in the initial-state radiation (ISR) and  
 476 the final-state radiation (FSR) is estimated from alternative MC samples with re-  
 477 duced or increased values for the strong coupling constant used by PYTHIA to gen-  
 478 erate initial- or final-state radiation. The scale in the ISR is varied by factors of 2 and  
 479 0.5, and the scale in the FSR by factors of  $\sqrt{2}$  and  $1/\sqrt{2}$  [58]. In the hadronic channel,  
 480 the FSR uncertainty is constrained by a fit to the data in the signal region  $SR_B$ , using  
 481 the NN output that is sensitive to the modelling of the FSR. This leads to a reduction  
 482 by a factor 0.3 relative to the variations from the alternative MC samples.
- 483 • **Matrix element – parton shower matching:** In the POWHEG matrix element to parton  
 484 shower (ME-PS) matching scheme, the resummation damping factor  $h_{\text{damp}}$  is used to  
 485 regulate high- $p_T$  radiation. The nominal value is  $h_{\text{damp}} = 1.58m_t$ , with  $m_t$  being the  
 486 generated top quark mass. Uncertainties in  $h_{\text{damp}}$  are parameterized by considering  
 487 alternative simulated samples with  $h_{\text{damp}} = m_t$  and  $h_{\text{damp}} = 2.24m_t$ .
- 488 • **Underlying event tune:** This uncertainty is estimated from alternative MC samples  
 489 with the tune CUETP8M2T4 parameters varied by  $\pm 1\sigma$ .

## 490 9 Cross section measurements

491 This section discusses the differential  $t\bar{t}$  production cross section measurements for the hadronic  
 492 and  $\ell$ +jets channels. The cross sections are measured as a function of different kinematic vari-  
 493 ables for the top quark or the  $t\bar{t}$  system, and are corrected to the particle and parton level using  
 494 an unfolding procedure. The measurements are compared to predictions from different MC  
 495 event generators and high-order calculations.

### 496 9.1 Definition of the particle and parton level

497 The parton-level phase space to which the measurement is unfolded is constrained by the kine-  
 498 matic requirements of the detector-level fiducial region. Namely, for the hadronic channel, the  
 499 top quark and antiquark must have  $p_T > 400 \text{ GeV}$  and  $|\eta| < 2.4$ , while the invariant mass of the  
 500  $t\bar{t}$  system must be greater than  $800 \text{ GeV}$  in order to avoid extreme events with high top quark  
 501  $p_T$  and very low  $m_{t\bar{t}}$ .

502 The parton-level definition for the  $\ell$ +jets channel differs from the hadronic channel because  
 503 the differential cross section is reported as a function of the hadronically decaying top quark.

504 Therefore, the parton-level phase space is confined to semileptonic events, where the  $p_T$  of the  
 505 hadronically decaying top quark is greater than 400 GeV, to match the fiducial requirement at  
 506 the detector level.

507 The so-called *particle level* represents the *state* that consists of *stable particles* originating from  
 508 the pp collision, *after the hadronization* process but *before the interaction* of these particles  
 509 with the *detector*. The observables computed from the particles' momenta are thought to be  
 510 better defined compared to the ones computed from parton-level information. Also, the associated  
 511 phase space is *closer to the fiducial phase space* of the measurement at the detector level,  
 512 which results in smaller theoretical uncertainties. In the context of this analysis, particle jets  
 513 are reconstructed from *stable particles*, excluding neutrinos, with the *anti- $k_T$*  algorithm using  
 514 a distance parameter of 0.8, identical to the detector-level reconstruction. Only particles origi-  
 515 nating from the *primary interaction* are considered. Subsequently, jets that are *geometrically*  
 516 *matched*, within  $\Delta R < 0.4$  in  $\eta - \phi$ , to generated leptons (i.e. from the leptonic decays of W  
 517 bosons) are *removed* from the *particle jet collection*. For the *hadronic channel*, the *two* parti-  
 518 cle jets with the *highest  $p_T$*  are considered the *particle-level t candidates*. In order to match as  
 519 closely as possible the fiducial phase space, the same kinematic selection criteria are applied as  
 520 for the detector-level events. In particular, the particle-level jets must have  $p_T > 400$  GeV and  
 521  $|\eta| < 2.4$ , while the mass of each jet should be in the range 120–220 GeV and the *invariant mass*  
 522 of the two jets be greater than 800 GeV. The *matching efficiency* between the *particle-level t*  
 523 candidates and the original top quarks at the *parton level* varies between 96% and 98%.

524 The *particle-level phase space* for the  $\ell + \text{jets}$  channel is set up to *mimic* the *kinematic selections*  
 525 at the *detector level*. Particle-level *large- $R$*  jets are selected if they fulfill  $p_T > 400$  GeV,  $|\eta| < 2.4$ ,  
 526 and  $105 < m_{\text{jet}} < 220$  GeV, and are then referred to as *particle-level t jets*. Particle-level *small- $R$*   
 527 jets are selected if they have  $p_T > 50$  GeV,  $|\eta| < 2.4$ , and are flagged as a *b jet*; these are  
 528 referred to as *particle-level b jets*. Particle-level *electrons* and *muons* are selected if they have  
 529  $p_T > 50$  GeV and  $|\eta| < 2.1$ . To fulfill the *particle-level selection criteria*, an event must contain  
 530 at least *one* *particle-level t jet*, at least *one* *particle-level b jet*, and at least *one* *particle-level*  
 531 *electron or muon*.

532 In order to quantify the overlap between the *detector-, particle-, and parton-level phase space*  
 533 definitions, two fractions,  $f_{1,2}$ , are used. Here  $f_1$  is defined as the fraction of *reconstructed*  
 534 *events* that are *accompanied* by a *selected event* at the *unfolded level* (*parton* or *particle*) in  
 535 the *same observable range*, whereas  $f_2$  is the *fraction* of *events* at the *unfolded level* that is  
 536 *accompanied* by a *selected reconstructed event*. Figures 8 and 9 show the aforementioned  
 537 fractions at the *parton* and *particle level*, respectively, for the *hadronic channel* as a function  
 538 of the *leading top quark  $p_T$*  and  $|y|$ . The  $f_1$  vs  $p_T$  shows a characteristic threshold behavior  
 539 due to the finite  $p_T$  resolution, while it is flat vs  $|y|$ . The  $f_2$  decreases vs  $p_T$ , primarily due to  
 540 the *subjet b tagging inefficiency* and the *NN output dependence* on the  $p_T$  (at high jet  $p_T$  it is  
 541 more difficult to differentiate between ordinary QCD jets and boosted top quarks). Also, the  $f_2$   
 542 decreases at high  $|y|$  values due to the increased *b tagging inefficiency* at the edges of the CMS  
 543 tracker detector.

a few words for the shapes of  $f_1, f_2$

## 544 9.2 Unfolding

545 To extract the differential cross sections at the *particle* and *parton level*, an unfolding method  
 546 is applied. Specifically, the *unfolded differential cross sections* are extracted according to

$$\frac{d\sigma_i^{\text{unf}}}{dx} = \frac{1}{\mathcal{L} \cdot \Delta x_i} \cdot \frac{1}{f_{2,i}} \cdot \sum_j \left( R_{ij}^{-1} \cdot f_{1,j} \cdot S_j \right), \quad (4)$$

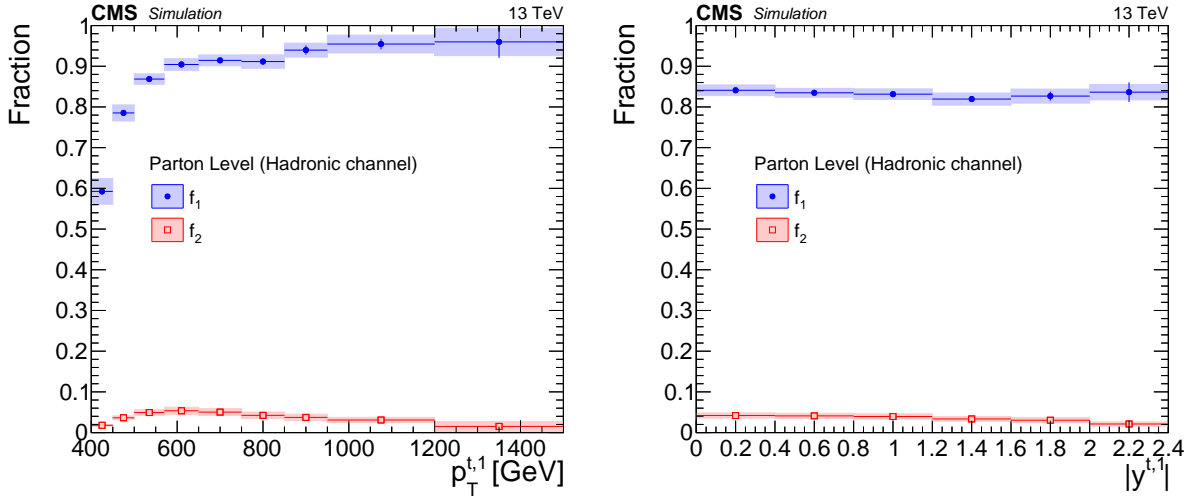


Figure 8: Simulated fractions  $f_{1,2}$  for the parton-level selection in the hadronic channel as a function of the leading top quark  $p_{\text{T}}$  and  $|y|$ .

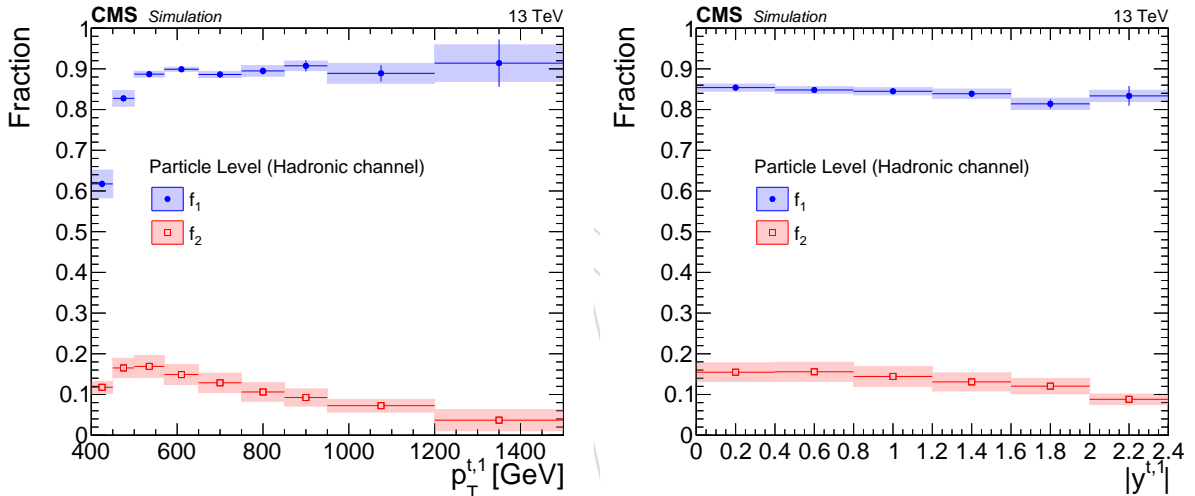


Figure 9: Simulated fractions  $f_{1,2}$  for the particle-level selection in the hadronic channel as a function of the leading top quark  $p_{\text{T}}$  and  $|y|$ .

547 where  $\mathcal{L}$  is the total integrated luminosity and  $\Delta x_i$  is the width of the  $i$ -th bin of the observable  
 548  $x$ . The quantity  $R_{ij}^{-1}$  is the inverse of the migration matrix between the  $i$ -th and  $j$ -th bins.  
 549 Due to the finite resolution of the detector, the migration matrix is non-diagonal and thus the  
 550 application of an unfolding procedure is necessary. The binning of the various observables has  
 551 been chosen such that the purity (fraction of reconstructed events for which the true value of the  
 552 observable lies in the same bin) and the stability (fraction of true events where the reconstructed  
 553 observable lies in the same bin) are well above 50%. This choice results in migration matrices  
 554 with suppressed non-diagonal elements, shown for the hadronic channel in Figs. 10 and 11, and  
 555 for the  $\ell + \text{jets}$  channel in Figs. 12 and 13. In order to avoid the biases introduced by the various  
 556 unfolding methods utilizing some type of regularization, the simple migration matrix inversion  
 557 is used, as written in Eq. 4, at a price of a moderate increase in the statistical uncertainty.

we use simple matrix inversion to avoid biases introduced  
by unfolding methods that utilise some type of regularization  
at a price of a moderate increase in the statistical uncertainty

why unfold?

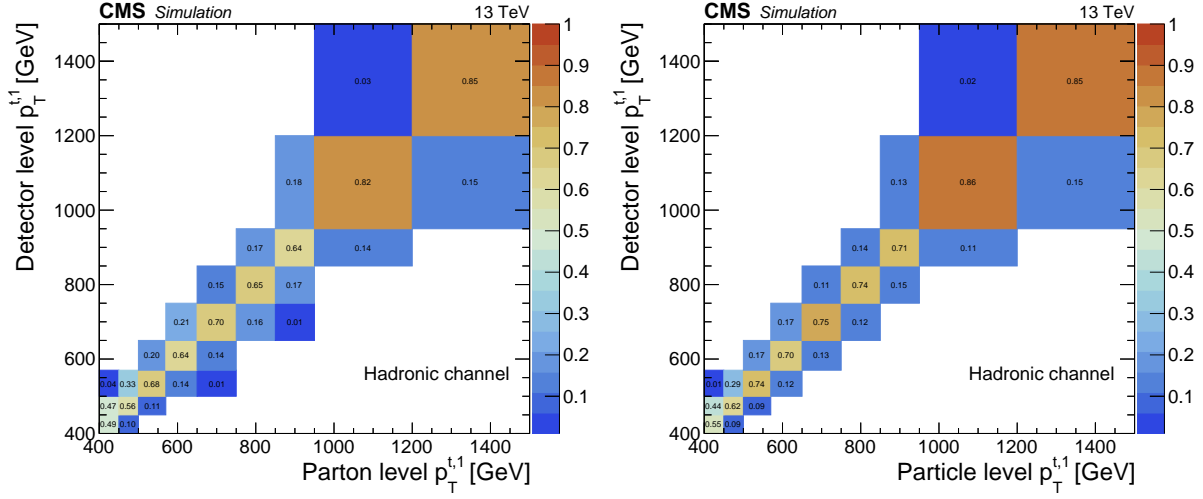


Figure 10: Simulated migration matrices for the leading top quark  $p_T$  at the parton level (left) and particle level (right) in the hadronic channel. Each column is normalized to unity.

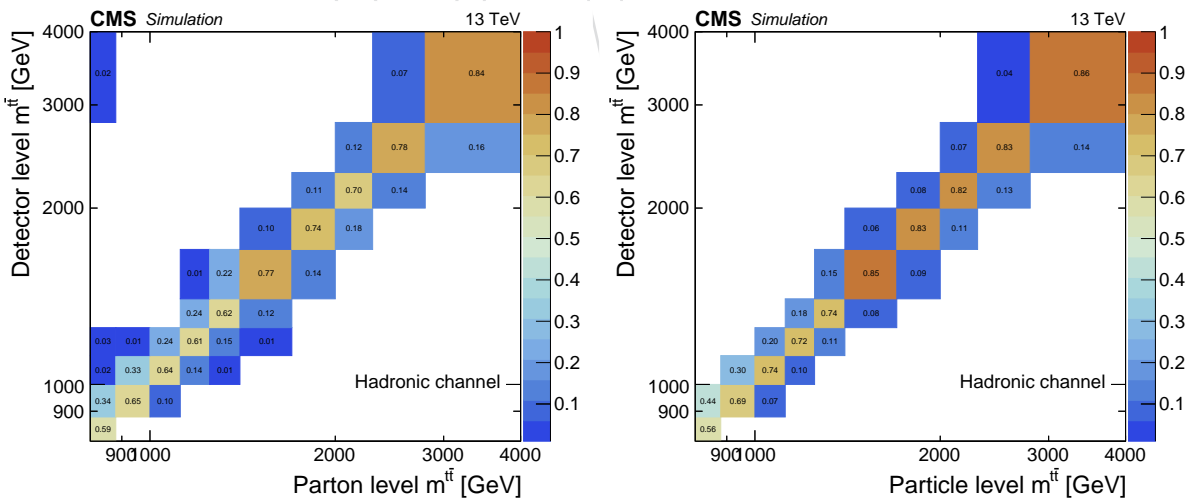


Figure 11: Simulated migration matrices for  $m_{t\bar{t}}$  at the parton level (left) and particle level (right) in the hadronic channel. Each column is normalized to unity.

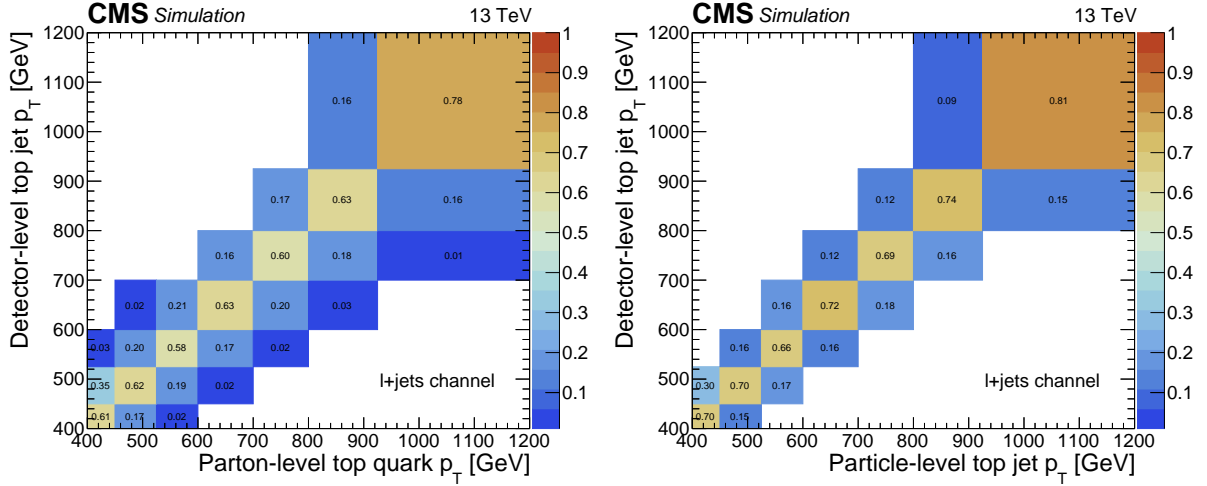


Figure 12: Simulated migration matrices for top quark  $p_T$  at the parton level (left) and particle level (right) in the  $\ell + \text{jets}$  channel. Each column is normalized to unity.

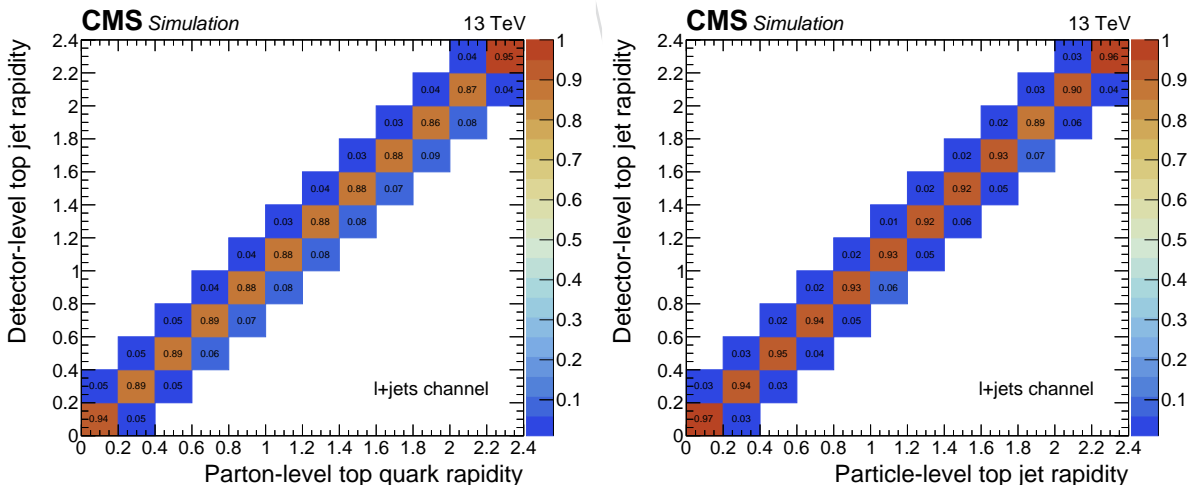


Figure 13: Simulated migration matrices for top quark rapidity at the parton level (left) and particle level (right) in the  $\ell + \text{jets}$  channel. Each column is normalized to unity.

### 558 9.3 Hadronic channel

559 For the hadronic channel, the measurement of the unfolded differential cross section in bin  $i$   
 560 of the variable  $x$  is performed using Eq. 4, where the signal yield  $S_i$  is computed from Eq. 3.  
 561 In order to estimate the uncertainty in the measurement, the entire procedure of the signal  
 562 extraction, unfolding with different response matrices, and extrapolation to the particle- or  
 563 parton-level phase space is repeated for every source of uncertainty discussed in Section 8. The  
 564 unfolded cross sections at the particle level are shown in Figs. 14–20 and at the parton level in  
 565 Figs. 21–27. Figures 28 and 29 show a summary of the statistical and the dominant systematic  
 566 uncertainties in the differential cross section measurements as a function of the leading top  
 567 quark  $p_T$  and  $|y|$  at the particle and parton level, respectively.

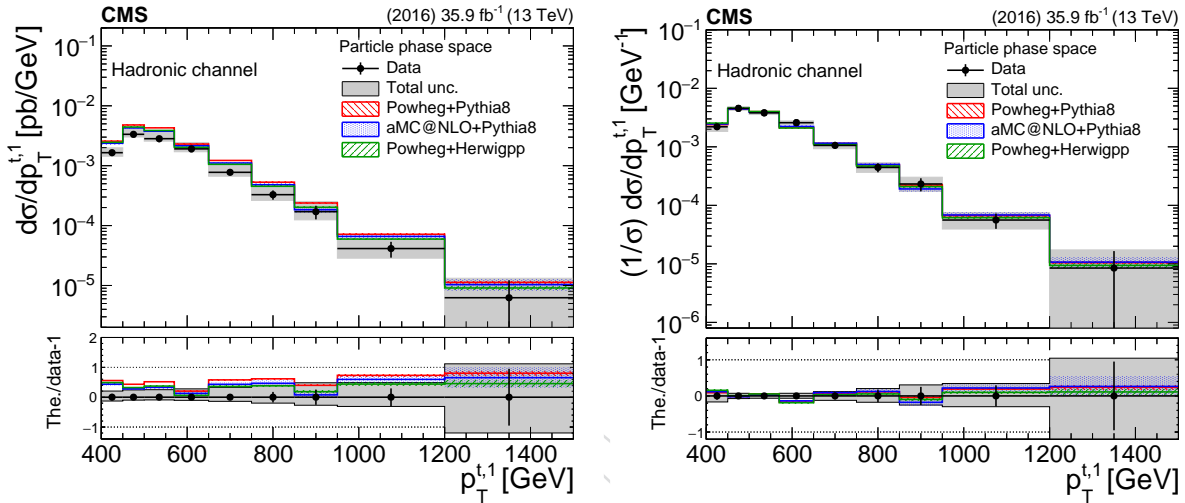


Figure 14: Differential cross section unfolded to the particle level, absolute (left) and normalized (right), as a function of the leading top quark  $p_T$  in the hadronic channel. The bottom panel shows the ratio (theory – data)/data. The uncertainties on the data markers are statistical, while the grey band shows the total statistical and systematic uncertainty.

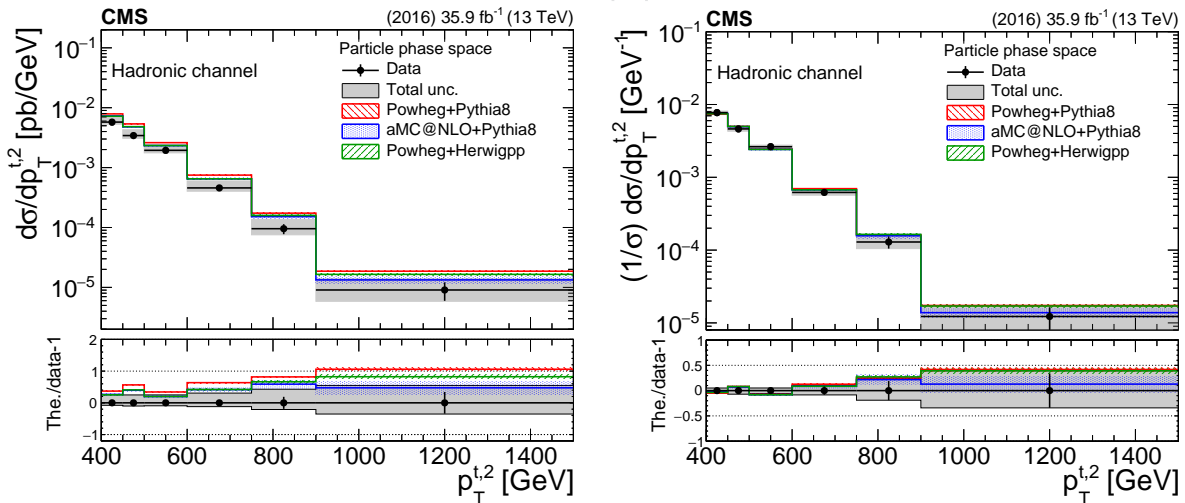


Figure 15: Differential cross section unfolded to the particle level, absolute (left) and normalized (right), as a function of the second top quark  $p_T$  in the hadronic channel. The bottom panel shows the ratio (theory – data)/data. The uncertainties on the data markers are statistical, while the grey band shows the total statistical and systematic uncertainty.

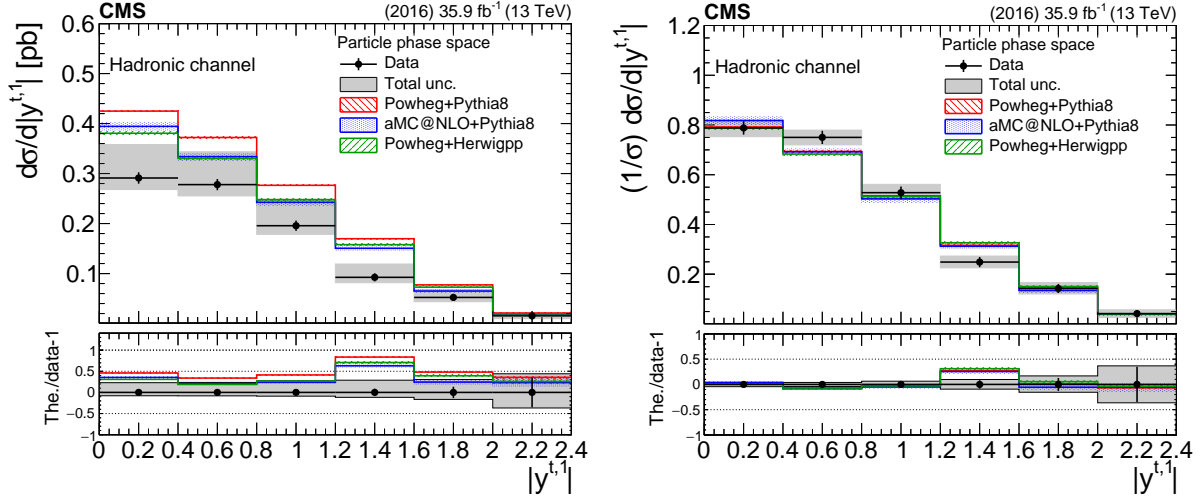


Figure 16: Differential cross section unfolded to the particle level, absolute (left) and normalized (right), as a function of the leading top quark  $|y|$  in the hadronic channel. The bottom panel shows the ratio (theory – data)/data. The uncertainties on the data markers are statistical, while the grey band shows the total statistical and systematic uncertainty.

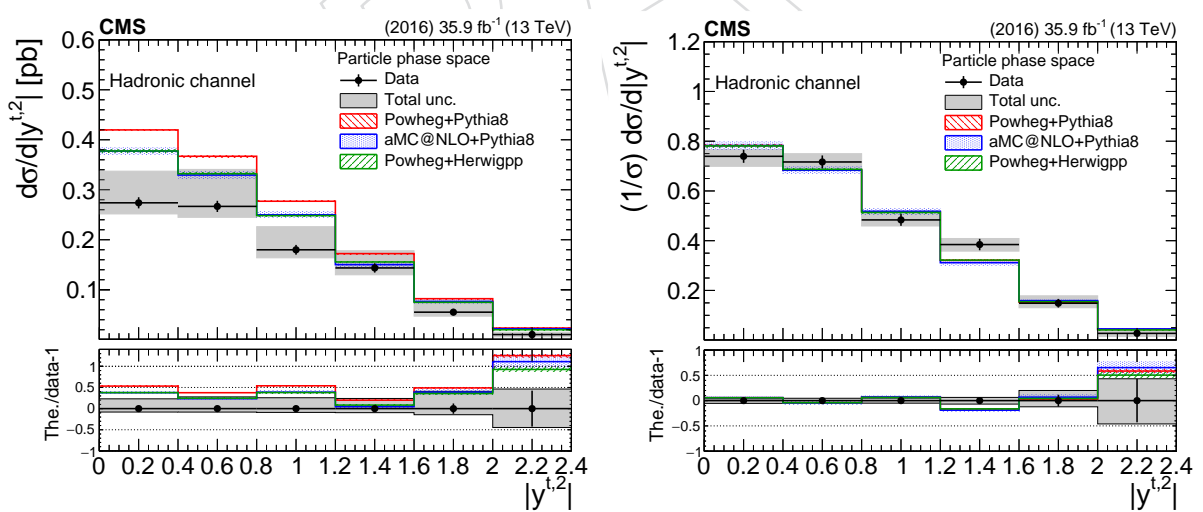


Figure 17: Differential cross section unfolded to the particle level, absolute (left) and normalized (right), as a function of the second top quark  $|y|$  in the hadronic channel. The bottom panel shows the ratio (theory – data)/data. The uncertainties on the data markers are statistical, while the grey band shows the total statistical and systematic uncertainty.

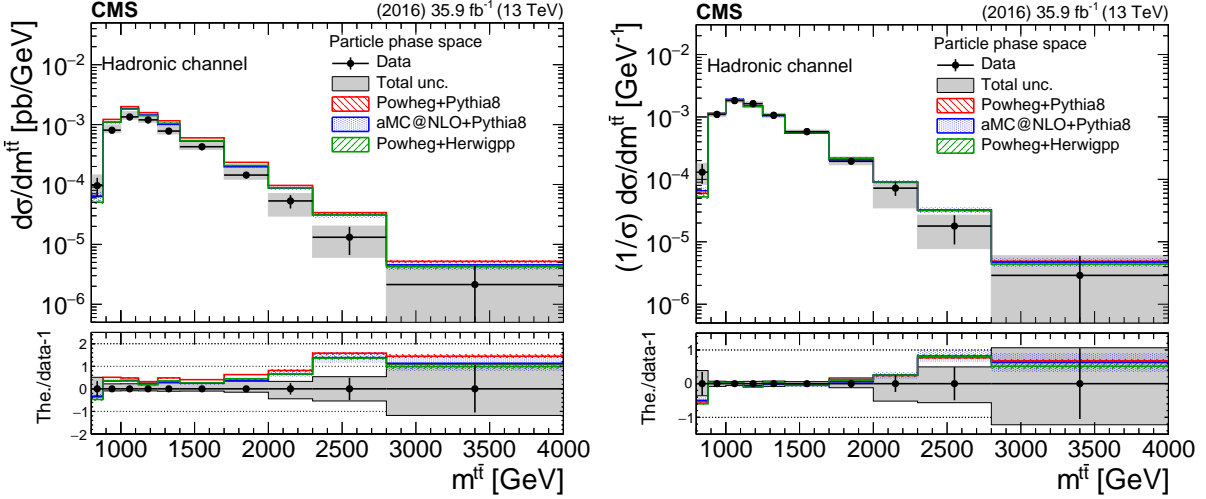


Figure 18: Differential cross section unfolded to the particle level, absolute (left) and normalized (right), as a function of  $m_{t\bar{t}}$  in the hadronic channel. The bottom panel shows the ratio (theory – data)/data. The uncertainties on the data markers are statistical, while the grey band shows the total statistical and systematic uncertainty.

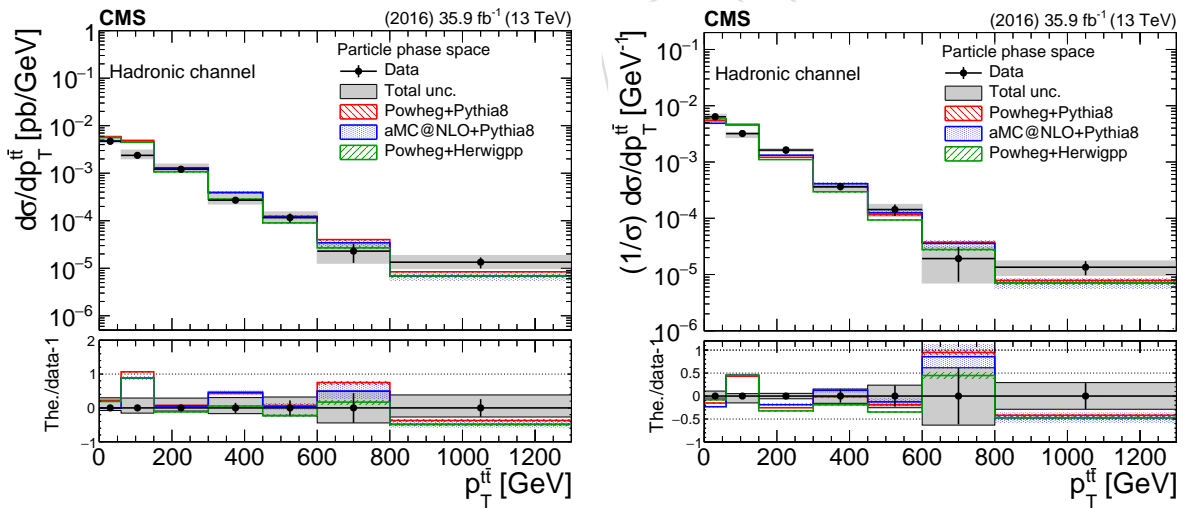


Figure 19: Differential cross section unfolded to the particle level, absolute (left) and normalized (right), as a function of  $p_T^{t\bar{t}}$  in the hadronic channel. The bottom panel shows the ratio (theory – data)/data. The uncertainties on the data markers are statistical, while the grey band shows the total statistical and systematic uncertainty.

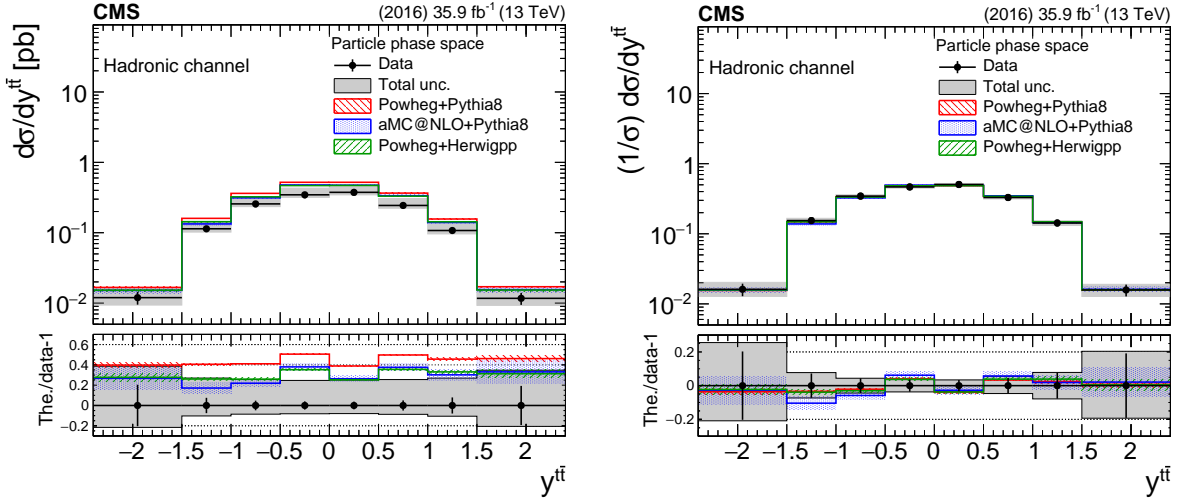


Figure 20: Differential cross section unfolded to the particle level, absolute (left) and normalized (right), as a function of  $y_{t\bar{t}}$  in the hadronic channel. The bottom panel shows the ratio (theory – data)/data. The uncertainties on the data markers are statistical, while the grey band shows the total statistical and systematic uncertainty.

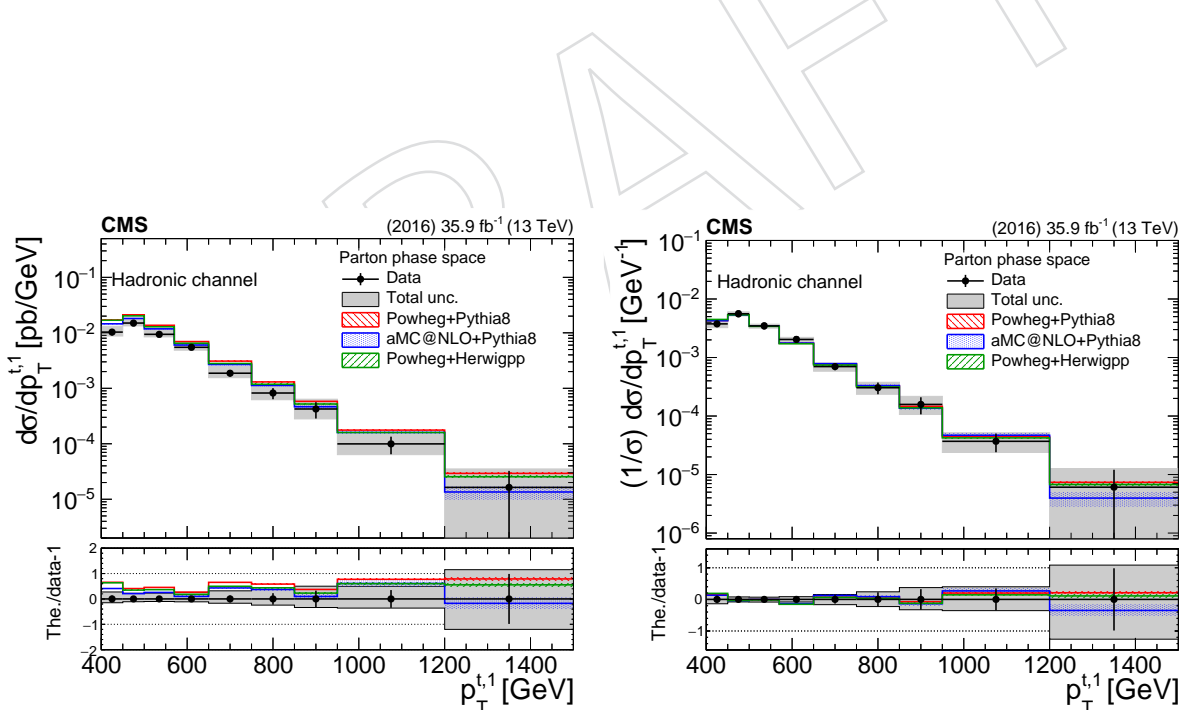


Figure 21: Differential cross section unfolded to the parton level, absolute (left) and normalized (right), as a function of the leading top quark  $p_T$  in the hadronic channel. The bottom panel shows the ratio (theory – data)/data. The uncertainties on the data markers are statistical, while the grey band shows the total statistical and systematic uncertainty.

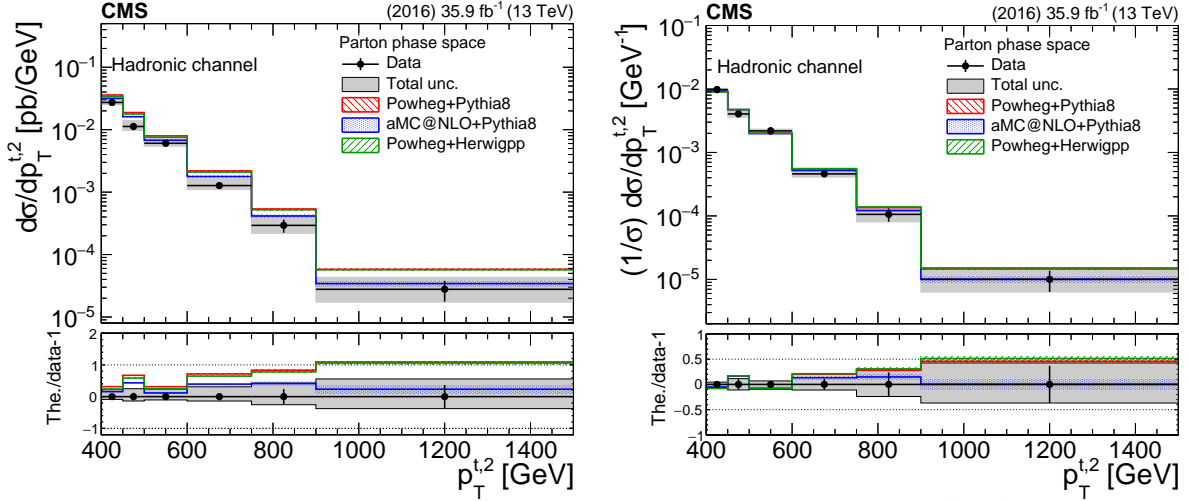


Figure 22: Differential cross section unfolded to the parton level, absolute (left) and normalized (right), as a function of the second top quark  $p_T$  in the hadronic channel. The bottom panel shows the ratio (theory – data)/data. The uncertainties on the data markers are statistical, while the grey band shows the total statistical and systematic uncertainty.

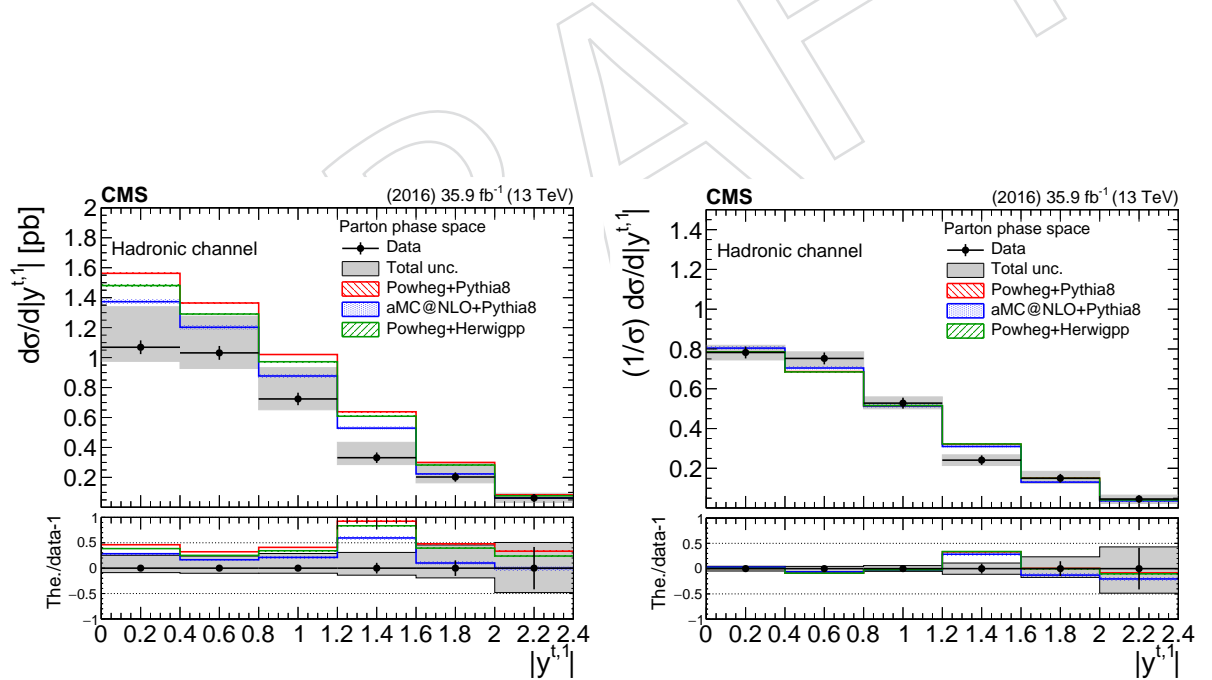


Figure 23: Differential cross section unfolded to the parton level, absolute (left) and normalized (right), as a function of the leading top  $|y|$  in the hadronic channel. The bottom panel shows the ratio (theory – data)/data. The uncertainties on the data markers are statistical, while the grey band shows the total statistical and systematic uncertainty.

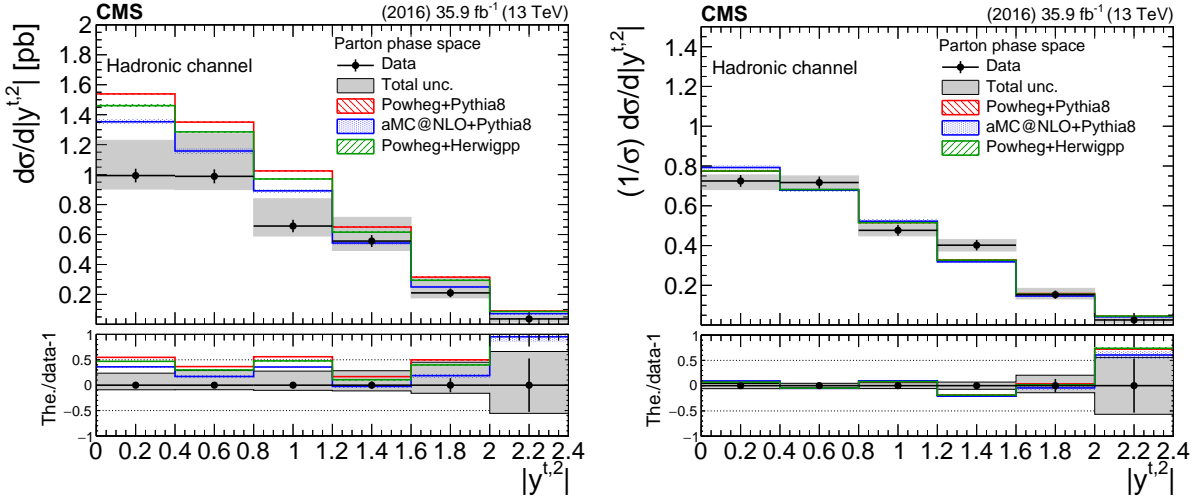


Figure 24: Differential cross section unfolded to the parton level, absolute (left) and normalized (right), as a function of the second top quark  $|y|$  in the hadronic channel. The bottom panel shows the ratio (theory – data)/data. The uncertainties on the data markers are statistical, while the grey band shows the total statistical and systematic uncertainty.

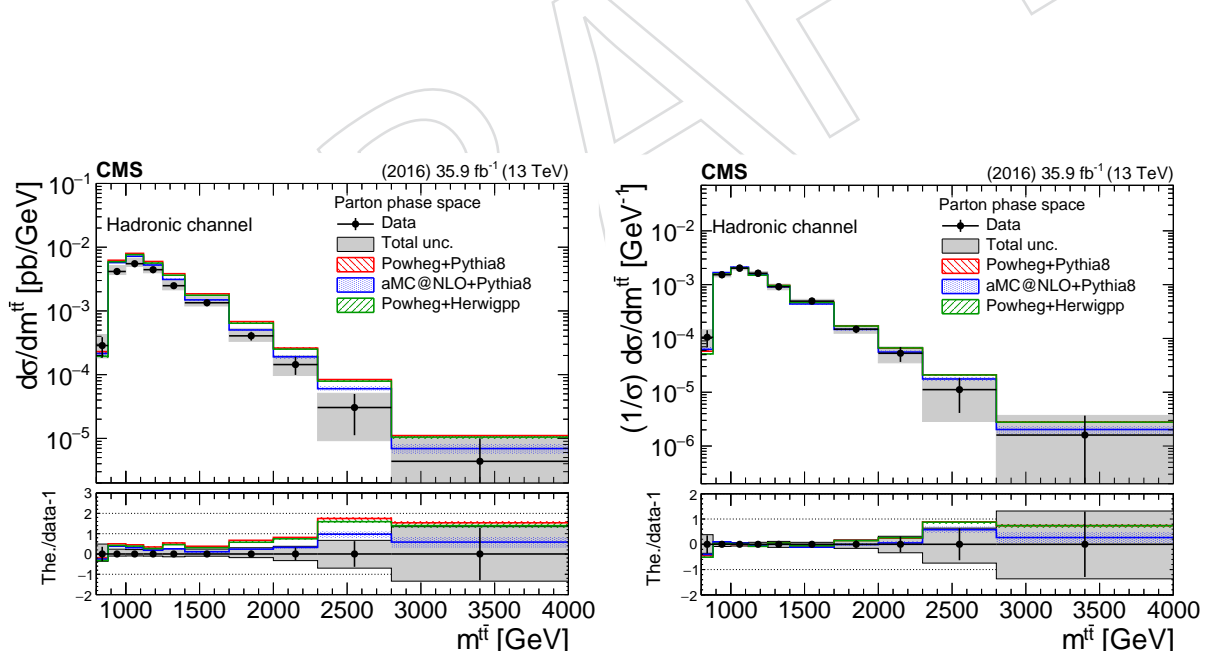


Figure 25: Differential cross section unfolded to the parton level, absolute (left) and normalized (right), as a function of  $m_{t\bar{t}}$  in the hadronic channel. The bottom panel shows the ratio (theory – data)/data. The uncertainties on the data markers are statistical, while the grey band shows the total statistical and systematic uncertainty.

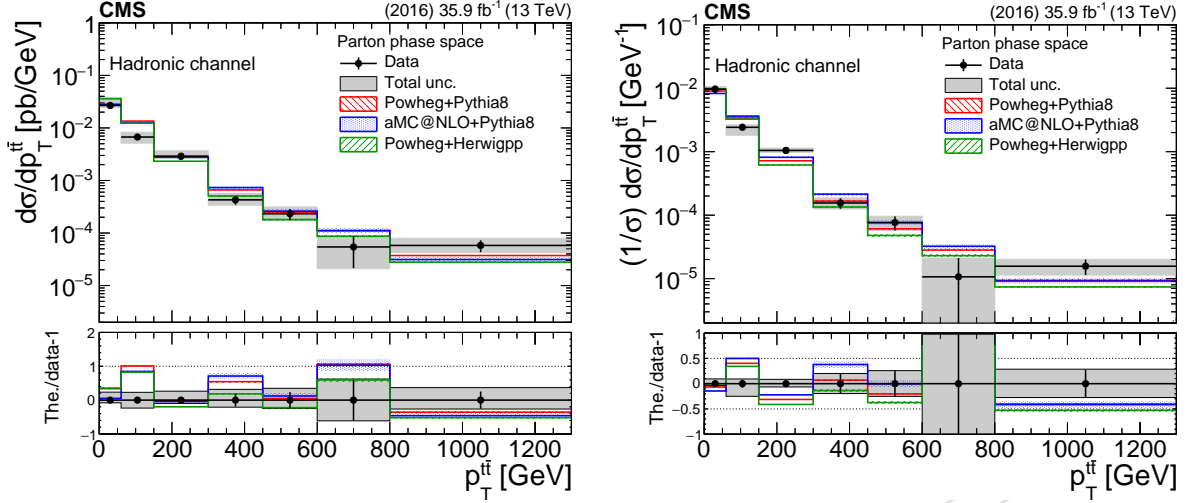


Figure 26: Differential cross section unfolded to the parton level, absolute (left) and normalized (right), as a function of  $p_T^{t\bar{t}}$  in the hadronic channel. The bottom panel shows the ratio (theory – data)/data. The uncertainties on the data markers are statistical, while the grey band shows the total statistical and systematic uncertainty.

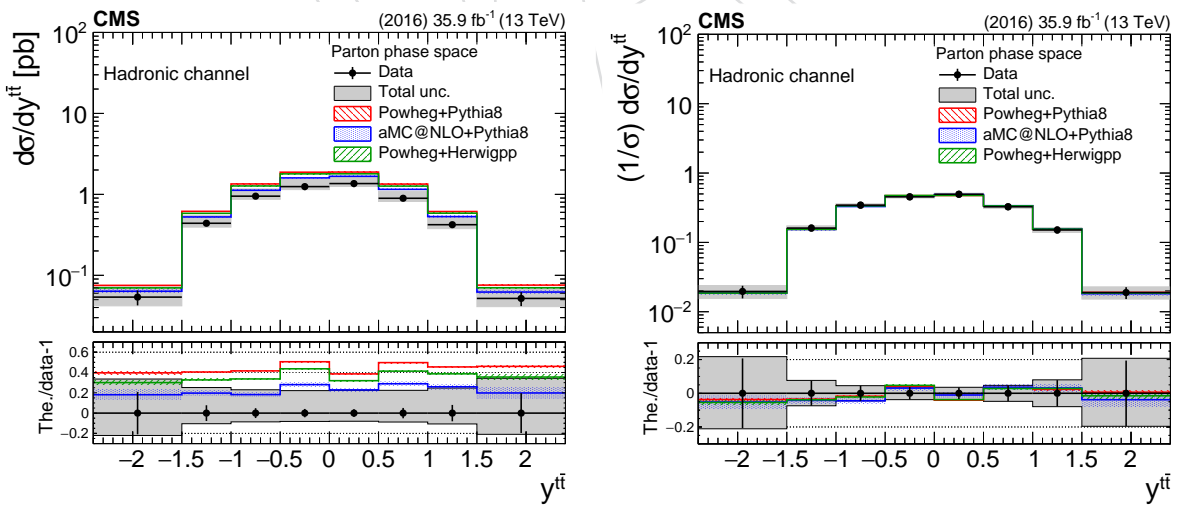


Figure 27: Differential cross section unfolded to the parton level, absolute (left) and normalized (right), as a function of  $y^{t\bar{t}}$  in the hadronic channel. The bottom panel shows the ratio (theory – data)/data. The uncertainties on the data markers are statistical, while the grey band shows the total statistical and systematic uncertainty.

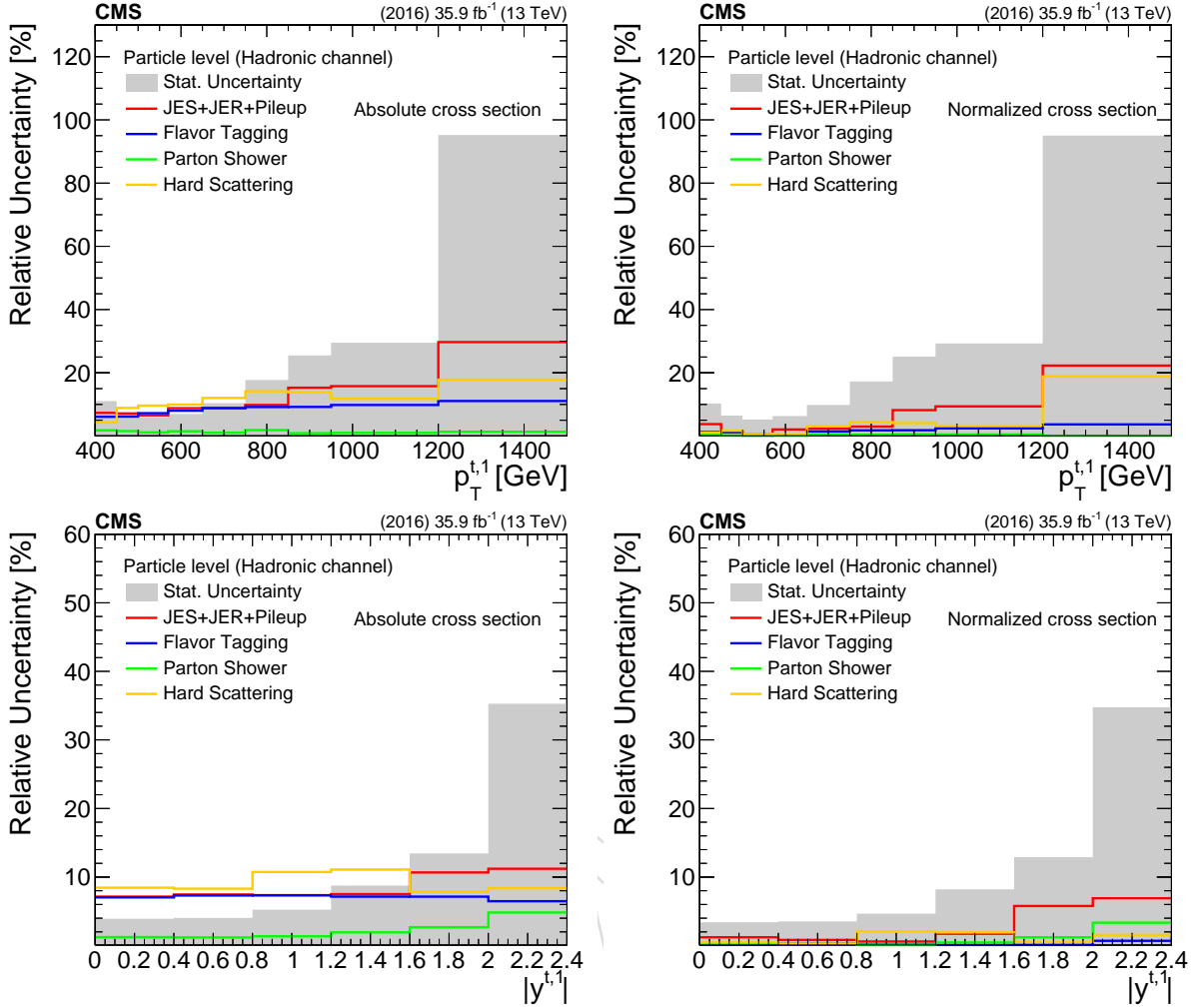


Figure 28: **Decomposition of uncertainties** in the **absolute** (left) and **normalized** (right) measurement at the **particle** level as a function of the leading top quark  $p_T$  (top) and  $|y|$  (bottom) in the hadronic channel. The grey band shows the statistical uncertainty, while the solid lines show the systematic uncertainties grouped in four categories: a) uncertainty due to pileup and the jet energy scale and resolution of the large- $R$  jets, b) uncertainty due to flavor tagging of the subjets, c) uncertainty due to the modeling of the parton shower, and d) uncertainty due to the modeling of the hard scattering.

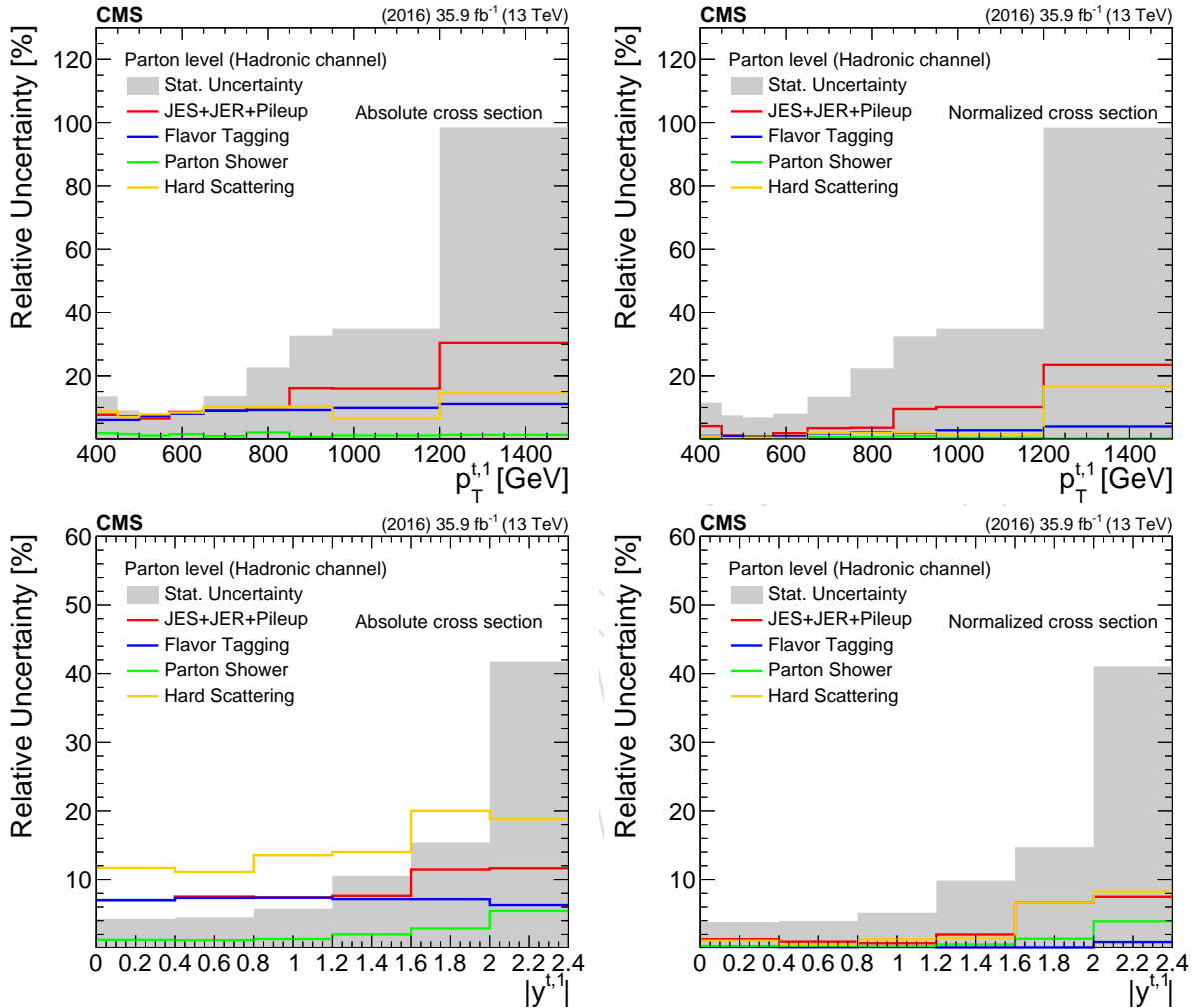


Figure 29: Decomposition of uncertainties in the absolute (left) and normalized (right) measurement at the parton level as a function of the leading top quark  $p_T$  (top) and  $|y|$  (bottom) in the hadronic channel. The grey band shows the statistical uncertainty, while the solid lines show the systematic uncertainties grouped in four categories: a) uncertainty due to pileup and the jet energy scale and resolution of the large- $R$  jets, b) uncertainty due to flavor tagging of the subjets, c) uncertainty due to the modeling of the parton shower, and d) uncertainty due to the modeling of the hard scattering.

568 **9.4 Lepton+jets channel**

569 In the  $\ell$ +jets channel, the differential  $t\bar{t}$  cross section is measured as a function of the  $p_T$  and  
 570  $|y|$  of the hadronically decaying top quark. The measurement is performed at the particle level  
 571 within a region of phase space mimicking the event selection criteria, as well as at the parton  
 572 level within the full phase space. Semileptonic  $t\bar{t}$  events are selected at the parton level, and the  
 573 properties of the hadronically decaying top quark are defined to represent the true top quark  
 574  $p_T$ .

575 The differential cross section is extracted from the signal-dominated 1t1b category. The mea-  
 576 sured signal distribution is determined by subtracting the estimated background contributions  
 577 from the distribution in data, using the posterior normalizations from the fit given in Table 3.  
 578 To account for signal reconstruction efficiencies and bin migrations, an unfolding procedure  
 579 based on a least squares minimization with Tikhonov regularization, as implemented in the  
 580 TUNFOLD framework, is applied [59]. An unregularized unfolding was found to be optimal for  
 581 the measurement. The unfolding relies on response matrices that map the  $p_T$  and  $|y|$  distribu-  
 582 tions for the t-tagged jet to corresponding properties for either the particle-level t jet candidate  
 583 or the parton-level top quark.

584 The systematic uncertainty in the unfolded measurement receives contributions from experi-  
 585 mental and theoretical sources, discussed in Section 8. The posterior values from the likelihood  
 586 fit are used for the t tagging efficiency, background normalizations, and lepton efficiencies,  
 587 while the a priori values are used for the remaining uncertainties. For each systematic vari-  
 588 ation that affects the shape of the  $p_T$  or  $|y|$  distribution, a separate response matrix is created  
 589 that is used to unfold the data. The resulting uncertainties are added in quadrature to obtain  
 590 the total uncertainty for the unfolded distribution.

591 The electron and muon channels are combined before the unfolding by merging the measured  
 592 distributions as well as the response matrices for the two channels. The background contribu-  
 593 tions are also merged before subtracting these from the measured distributions, with the  
 594 exception of the electron and muon QCD multijet backgrounds that are treated as separate  
 595 sources.

merge both  
e/muon  
channels

596 The unfolded cross section results are shown in Figs. 30–33 as a function of  $p_T$  and  $|y|$  for the  
 597 particle and parton level, respectively. The measurements are compared to the prediction from  
 598 POWHEG+PYTHIA 8. The breakdown of the sources of systematic uncertainty are shown in  
 599 Figs. 34 and 35. The unfolded cross section as a function of the  $p_T$  of the hadronically decaying  
 600 top quark at the parton level that is presented in this paper can additionally be compared to the  
 601 corresponding measurement from the CMS Collaboration in the resolved final state [16]. The  
 602 two measurements are observed to be in agreement in the region of phase space where they  
 603 overlap.

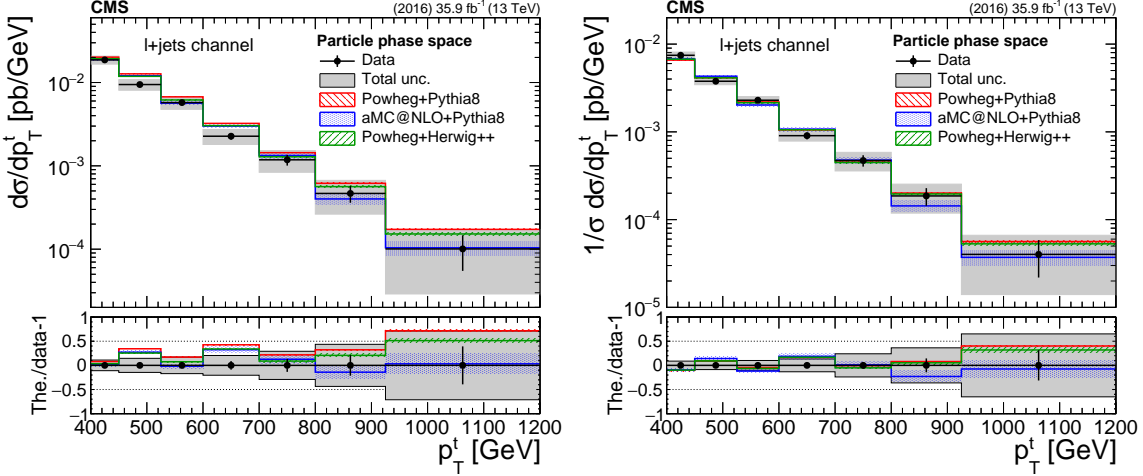


Figure 30: Differential cross section measurements at the particle level as a function of the particle-level  $t$  jet  $p_T$  for the  $\ell + \text{jets}$  channel. Both absolute (left) and normalized (right) cross sections are shown. The uncertainties on the data markers are statistical, while the grey band shows the total statistical and systematic uncertainty.

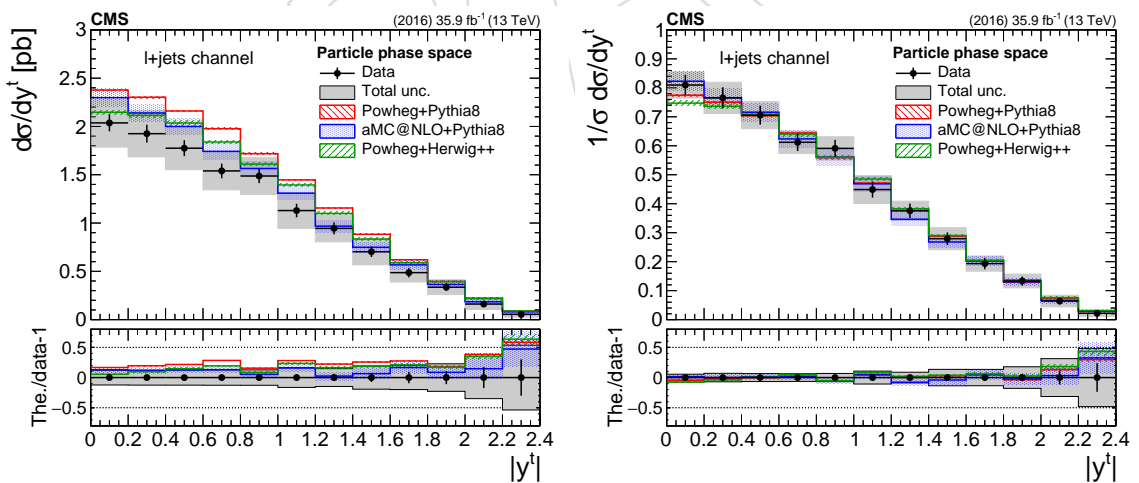


Figure 31: Differential cross section measurements at the particle level as a function of the particle-level  $t$  jet  $|y|$  for the  $\ell + \text{jets}$  channel. Both absolute (left) and normalized (right) cross sections are shown. The uncertainties on the data markers are statistical, while the grey band shows the total statistical and systematic uncertainty.

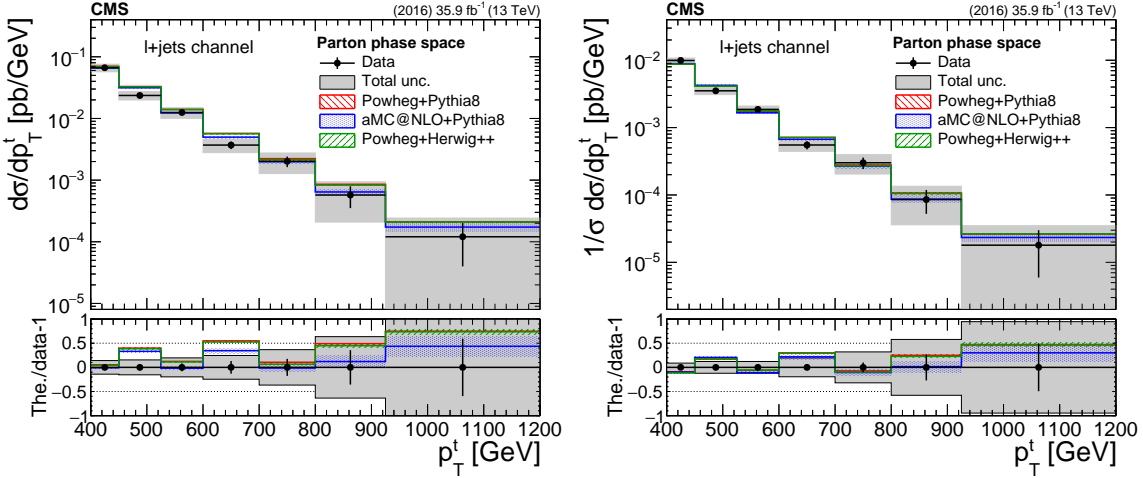


Figure 32: Differential cross section measurements at the parton level as a function of the parton-level top quark  $p_T$  for the  $\ell$ +jets channel. Both absolute (left) and normalized (right) cross sections are shown. The uncertainties on the data markers are statistical, while the grey band shows the total statistical and systematic uncertainty.

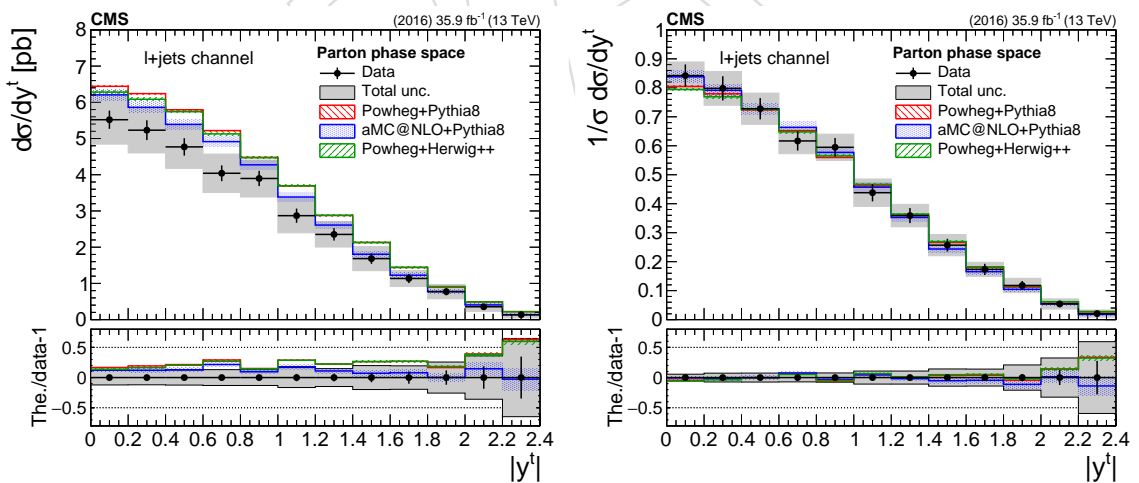


Figure 33: Differential cross section measurements at the parton level as a function of the parton-level top quark  $|y|$  for the  $\ell$ +jets channel. Both absolute (left) and normalized (right) cross sections are shown. The uncertainties on the data markers are statistical, while the grey band shows the total statistical and systematic uncertainty.

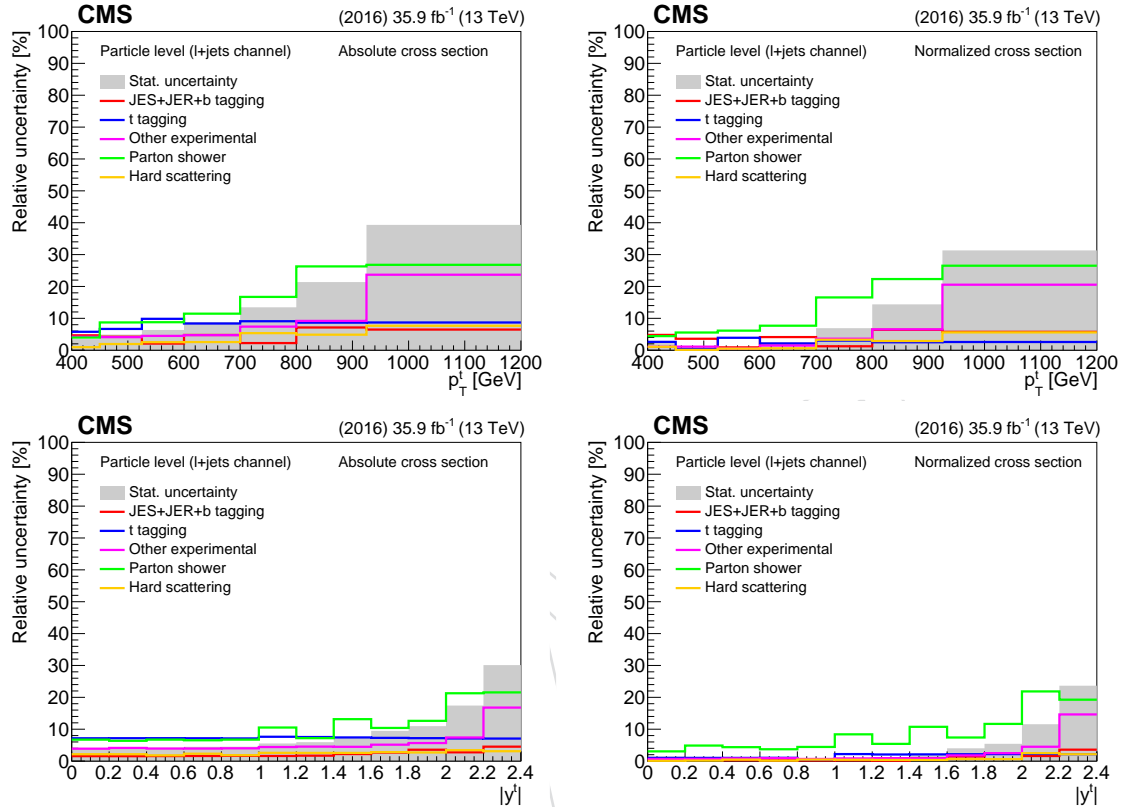


Figure 34: Breakdown of the sources of systematic uncertainty affecting the differential cross section measurements in the  $\ell$ +jets channel at the particle level as a function of the particle-level  $t$  jet  $p_T$  (top row) or  $|y|$  (bottom row). Both the systematic uncertainties in the absolute (left column) and the normalized (right column) cross sections are shown. "JES+JER+b tagging" includes uncertainties due to the jet energy scale, jet energy resolution, and small- $R$  jet  $b$  tagging efficiency; " $t$  tagging" is the uncertainty associated with the large- $R$  jet  $t$  tagging efficiency; "Other experimental" includes the uncertainties originating from the background estimate, pileup modeling, lepton identification and trigger efficiency, and measurement of the integrated luminosity; "Parton shower" includes contributions from initial- and final-state radiation, underlying event tune, ME-PS matching, and color reconnection; "Hard scattering" includes the uncertainty due to PDFs as well as renormalization and factorization scales.

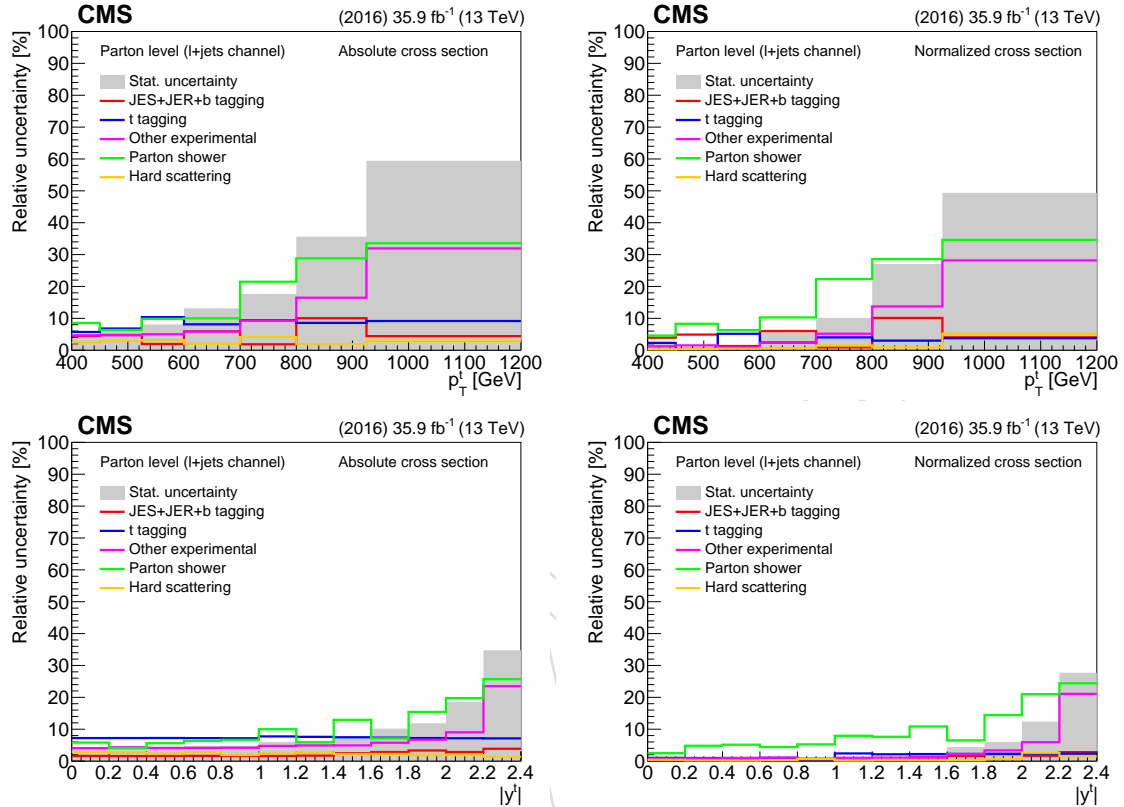


Figure 35: Breakdown of the sources of systematic uncertainty affecting the differential cross section measurements in the  $\ell$ +jets channel at the parton level as a function of the top quark  $p_T$  (top row) or  $|y|$  (bottom row). Both the systematic uncertainties in the absolute (left column) and the normalized (right column) cross sections are shown. "JES+JER+b tagging" includes uncertainties due to the jet energy scale, jet energy resolution, and small- $R$  jet b tagging efficiency; "t tagging" is the uncertainty associated with the large- $R$  jet t tagging efficiency; "Other experimental" includes the uncertainties originating from the background estimate, pileup modeling, lepton identification and trigger efficiency, and measurement of the integrated luminosity; "Parton shower" includes contributions from initial- and final-state radiation, underlying event tune, ME-PS matching, and color reconnection; "Hard scattering" includes the uncertainty due to PDFs as well as renormalization and factorization scales.

---

**604 9.5 Discussion**

605 The unfolded cross sections at the particle and parton level presented in Section 9 reveal some  
 606 interesting features. First, there is a significant overestimate of the integrated cross section  
 607 by about 35 (25)% in the hadronic ( $\ell$ +jets) channel, which is also in agreement with previous  
 608 results [17]. In terms of the normalized differential cross section distributions, there is good  
 609 agreement between the data and theory predictions for the leading top quark (hadronic chan-  
 610 nel) and the hadronically decaying top quark ( $\ell$ +jets channel)  $p_T$ , while the cross section as a  
 611 function of the second top  $p_T$  (hadronic channel) appears to be softer in data for the POWHEG  
 612 predictions with MC@NLO providing the best description. The  $y$  distributions are described  
 613 well by the theory predictions in both channels. Finally, the measured  $t\bar{t}$  system kinematic  
 614 distributions are in agreement with the theory prediction, with a possible deviation in the  $m_{t\bar{t}}$   
 615 variable, where POWHEG tends to produce a harder spectrum while MC@NLO is fully consis-  
 616 tent with the data. Regarding the systematic uncertainties, it should be noted that they are in  
 617 general larger for the hadronic channel because the two leading experimental sources, due to  
 618 the jet energy scale and the b tagging, enter twice (two large- $R$  jets). In contrast, the parton-  
 619 shower uncertainty is smaller for the hadronic channel because its main contribution (FSR) is  
 620 constrained through a dedicated analysis, as explained in Section 8.

**621 10 Summary**

622 A measurement of the  $t\bar{t}$  production cross section for high- $p_T$  top quarks in proton-proton col-  
 623 lisions at 13 TeV has been presented. The measurement uses events where either one or both  
 624 top quarks decay hadronically, and where the hadronic decay products cannot be resolved but  
 625 are instead clustered in a single large- $R$  jet with  $p_T > 400$  GeV. The hadronic final state con-  
 626 tains two such large- $R$  jets, while the  $\ell$ +jets final state is identified through the presence of an  
 627 electron/muon, a b-tagged jet from the leptonically decaying top quark, missing transverse  
 628 momentum from the escaping neutrino, and a single t-tagged large- $R$  jet. The measurement  
 629 utilizes a larger data set compared to previous results in order to explore a wider phase space  
 630 of the  $t\bar{t}$  production and elucidate the discrepancies with the theory predictions that have been  
 631 reported in earlier publications. For the hadronic channel, absolute and normalized differential  
 632 cross section are presented as a function of the leading and subleading top quark  $p_T$  and  $|y|$ ,  
 633 and as a function of the invariant mass,  $p_T$ , and  $y$  of the  $t\bar{t}$  system, unfolded to the particle  
 634 and parton level. For the  $\ell$ +jets channel, the differential cross section is measured as a function  
 635 of the  $p_T$  and  $|y|$  of the hadronically decaying top quark, at the particle level within a fiducial  
 636 phase space and at the parton level. The results are compared to theoretical predictions from  
 637 the POWHEG matrix-element generator, interfaced with PYTHIA8 or HERWIG++ for the under-  
 638 lying event and parton shower, and from the MC@NLO matrix-element generator, interfaced  
 639 with PYTHIA8. All the models overpredict significantly the absolute cross section in the phase  
 640 space of the measurement (by up to 35%), while they describe consistently the differential dis-  
 641 tribution of most variables. The most notable discrepancy is observed for the hadronic channel  
 642 in the invariant mass of the  $t\bar{t}$  system and the  $p_T$  of the subleading t jet, where the theoretical  
 643 models predict a higher cross section at high mass and  $p_T$  values, respectively. To further inves-  
 644 tigate the severity of this discrepancy, more data is needed to enhance the statistical significance  
 645 of the measurement in this region of phase space.

## 646 Acknowledgements

647 We congratulate our colleagues in the CERN accelerator departments for the excellent perfor-  
648 mance of the LHC and thank the technical and administrative staffs at CERN and at other CMS  
649 institutes for their contributions to the success of the CMS effort. In addition, we gratefully  
650 acknowledge the computing centres and personnel of the Worldwide LHC Computing Grid  
651 for delivering so effectively the computing infrastructure essential to our analyses. Finally, we  
652 acknowledge the enduring support for the construction and operation of the LHC and the CMS  
653 detector provided by the following funding agencies: the Austrian Federal Ministry of Educa-  
654 tion, Science and Research and the Austrian Science Fund; the Belgian Fonds de la Recherche  
655 Scientifique, and Fonds voor Wetenschappelijk Onderzoek; the Brazilian Funding Agencies  
656 (CNPq, CAPES, FAPERJ, FAPERGS, and FAPESP); the Bulgarian Ministry of Education and  
657 Science; CERN; the Chinese Academy of Sciences, Ministry of Science and Technology, and Na-  
658 tional Natural Science Foundation of China; the Colombian Funding Agency (COLCIENCIAS);  
659 the Croatian Ministry of Science, Education and Sport, and the Croatian Science Foundation;  
660 the Research Promotion Foundation, Cyprus; the Secretariat for Higher Education, Science,  
661 Technology and Innovation, Ecuador; the Ministry of Education and Research, Estonian Re-  
662 search Council via IUT23-4 and IUT23-6 and European Regional Development Fund, Estonia;  
663 the Academy of Finland, Finnish Ministry of Education and Culture, and Helsinki Institute of  
664 Physics; the Institut National de Physique Nucléaire et de Physique des Particules / CNRS, and  
665 Commissariat à l’Énergie Atomique et aux Énergies Alternatives / CEA, France; the Bundes-  
666 ministerium für Bildung und Forschung, Deutsche Forschungsgemeinschaft, and Helmholtz-  
667 Gemeinschaft Deutscher Forschungszentren, Germany; the General Secretariat for Research  
668 and Technology, Greece; the National Research, Development and Innovation Fund, Hungary;  
669 the Department of Atomic Energy and the Department of Science and Technology, India; the  
670 Institute for Studies in Theoretical Physics and Mathematics, Iran; the Science Foundation, Ire-  
671 land; the Istituto Nazionale di Fisica Nucleare, Italy; the Ministry of Science, ICT and Future  
672 Planning, and National Research Foundation (NRF), Republic of Korea; the Ministry of Educa-  
673 tion and Science of the Republic of Latvia; the Lithuanian Academy of Sciences; the Ministry  
674 of Education, and University of Malaya (Malaysia); the Ministry of Science of Montenegro; the  
675 Mexican Funding Agencies (BUAP, CINVESTAV, CONACYT, LNS, SEP, and UASLP-FAI); the  
676 Ministry of Business, Innovation and Employment, New Zealand; the Pakistan Atomic Energy  
677 Commission; the Ministry of Science and Higher Education and the National Science Centre,  
678 Poland; the Fundação para a Ciência e a Tecnologia, Portugal; JINR, Dubna; the Ministry of  
679 Education and Science of the Russian Federation, the Federal Agency of Atomic Energy of the  
680 Russian Federation, Russian Academy of Sciences, the Russian Foundation for Basic Research,  
681 and the National Research Center “Kurchatov Institute”; the Ministry of Education, Science  
682 and Technological Development of Serbia; the Secretaría de Estado de Investigación, Desar-  
683 rollo e Innovación, Programa Consolider-Ingenio 2010, Plan Estatal de Investigación Científica  
684 y Técnica y de Innovación 2013–2016, Plan de Ciencia, Tecnología e Innovación 2013–2017 del  
685 Principado de Asturias, and Fondo Europeo de Desarrollo Regional, Spain; the Ministry of  
686 Science, Technology and Research, Sri Lanka; the Swiss Funding Agencies (ETH Board, ETH  
687 Zurich, PSI, SNF, UniZH, Canton Zurich, and SER); the Ministry of Science and Technology,  
688 Taipei; the Thailand Center of Excellence in Physics, the Institute for the Promotion of Teach-  
689 ing Science and Technology of Thailand, Special Task Force for Activating Research and the  
690 National Science and Technology Development Agency of Thailand; the Scientific and Tech-  
691 nical Research Council of Turkey, and Turkish Atomic Energy Authority; the National Academy  
692 of Sciences of Ukraine, and State Fund for Fundamental Researches, Ukraine; the Science and  
693 Technology Facilities Council, UK; the US Department of Energy, and the US National Science  
694 Foundation.

695 Individuals have received support from the Marie-Curie programme and the European Re-  
 696 search Council and Horizon 2020 Grant, contract Nos. 675440 and 765710 (European Union);  
 697 the Leventis Foundation; the A.P. Sloan Foundation; the Alexander von Humboldt Foundation;  
 698 the Belgian Federal Science Policy Office; the Fonds pour la Formation à la Recherche dans  
 699 l'Industrie et dans l'Agriculture (FRIA-Belgium); the Agentschap voor Innovatie door Wetens-  
 700 chap en Technologie (IWT-Belgium); the F.R.S.-FNRS and FWO (Belgium) under the "Excel-  
 701 lence of Science – EOS" – be.h project n. 30820817; the Beijing Municipal Science & Technology  
 702 Commission, No. Z181100004218003; the Ministry of Education, Youth and Sports (MEYS) of  
 703 the Czech Republic; the Lendület ("Momentum") Programme and the János Bolyai Research  
 704 Scholarship of the Hungarian Academy of Sciences, the New National Excellence Program  
 705 ÚNKP, the NKFIA research grants 123842, 123959, 124845, 124850, and 125105 (Hungary); the  
 706 Council of Scientific and Industrial Research, India; the HOMING PLUS programme of the  
 707 Foundation for Polish Science, cofinanced from European Union, Regional Development Fund,  
 708 the Mobility Plus programme of the Ministry of Science and Higher Education, the National  
 709 Science Center (Poland), contracts Harmonia 2014/14/M/ST2/00428, Opus 2014/13/B/ST2/02543,  
 710 2014/15/B/ST2/03998, and 2015/19/B/ST2/02861, Sonata-bis 2012/07/E/ST2/01406; the Na-  
 711 tional Priorities Research Program by Qatar National Research Fund; the Programa de Excelen-  
 712 cia María de Maeztu, and the Programa Severo Ochoa del Principado de Asturias; the Thalis  
 713 and Aristeia programmes cofinanced by EU-ESF and the Greek NSRF; the Rachadapisek Som-  
 714 pot Fund for Postdoctoral Fellowship, Chulalongkorn University, and the Chulalongkorn Aca-  
 715 demic into Its 2nd Century Project Advancement Project (Thailand); the Welch Foundation,  
 716 contract C-1845; and the Weston Havens Foundation (USA).

## 717 References

- 718 [1] ATLAS Collaboration, "Measurements of top-quark pair differential cross-sections in the  
 719 lepton+jets channel in  $pp$  collisions at  $\sqrt{s} = 13$  TeV using the ATLAS detector", *JHEP* **11**  
 720 (2017) 191, doi:10.1007/JHEP11(2017)191, arXiv:1708.00727.
- 721 [2] ATLAS Collaboration, "Measurements of top-quark pair differential cross-sections in the  
 722  $e\mu$  channel in  $pp$  collisions at  $\sqrt{s} = 13$  TeV using the ATLAS detector", *Eur. Phys. J.* **C77**  
 723 (2017) 292, doi:10.1140/epjc/s10052-017-4821-x, arXiv:1612.05220.
- 724 [3] ATLAS Collaboration, "Measurement of lepton differential distributions and the top  
 725 quark mass in  $t\bar{t}$  production in  $pp$  collisions at  $\sqrt{s} = 8$  TeV with the ATLAS detector",  
 726 *Eur. Phys. J.* **C77** (2017) 804, doi:10.1140/epjc/s10052-017-5349-9,  
 727 arXiv:1709.09407.
- 728 [4] ATLAS Collaboration, "Measurement of top quark pair differential cross-sections in the  
 729 dilepton channel in  $pp$  collisions at  $\sqrt{s} = 7$  and 8 TeV with ATLAS", *Phys. Rev.* **D94**  
 730 (2016) 092003, doi:10.1103/PhysRevD.94.092003, arXiv:1607.07281.
- 731 [5] ATLAS Collaboration, "Differential top-antitop cross-section measurements as a function  
 732 of observables constructed from final-state particles using  $pp$  collisions at  $\sqrt{s} = 7$  TeV in  
 733 the ATLAS detector", *JHEP* **06** (2015) 100, doi:10.1007/JHEP06(2015)100,  
 734 arXiv:1502.05923.
- 735 [6] ATLAS Collaboration, "Measurements of top quark pair relative differential  
 736 cross-sections with ATLAS in  $pp$  collisions at  $\sqrt{s} = 7$  TeV", *Eur. Phys. J.* **C73** (2013) 2261,  
 737 doi:10.1140/epjc/s10052-012-2261-1, arXiv:1207.5644.

- [7] CMS Collaboration, "Measurement of normalized differential  $t\bar{t}$  cross sections in the dilepton channel from pp collisions at  $\sqrt{s} = 13$  TeV", *JHEP* **04** (2018) 060, doi:10.1007/JHEP04(2018)060, arXiv:1708.07638.
- [8] CMS Collaboration, "Measurements of normalised multi-differential cross sections for top quark pair production in pp collisions at  $\sqrt{s} = 13$  TeV and simultaneous determination of the strong coupling strength, top quark pole mass and parton distribution functions", (2019). arXiv:1904.05237. Submitted to *Eur. Phys. J.*
- [9] CMS Collaboration, "Measurements of  $t\bar{t}$  differential cross sections in proton-proton collisions at  $\sqrt{s} = 13$  TeV using events containing two leptons", *JHEP* **02** (2019) 149, doi:10.1007/JHEP02(2019)149, arXiv:1811.06625.
- [10] CMS Collaboration, "Measurement of differential cross sections for top quark pair production using the lepton+jets final state in proton-proton collisions at 13 TeV", *Phys. Rev.* **D95** (2017) 092001, doi:10.1103/PhysRevD.95.092001, arXiv:1610.04191.
- [11] CMS Collaboration, "Measurements of differential cross sections of top quark pair production as a function of kinematic event variables in proton-proton collisions at  $\sqrt{s} = 13$  TeV", *JHEP* **06** (2018) 002, doi:10.1007/JHEP06(2018)002, arXiv:1803.03991.
- [12] CMS Collaboration, "Measurement of double-differential cross sections for top quark pair production in pp collisions at  $\sqrt{s} = 8$  TeV and impact on parton distribution functions", *Eur. Phys. J.* **C77** (2017) 459, doi:10.1140/epjc/s10052-017-4984-5, arXiv:1703.01630.
- [13] CMS Collaboration, "Measurement of the differential cross section for top quark pair production in pp collisions at  $\sqrt{s} = 8$  TeV", *Eur. Phys. J.* **C75** (2015) 542, doi:10.1140/epjc/s10052-015-3709-x, arXiv:1505.04480.
- [14] CMS Collaboration, "Measurement of the differential cross sections for top quark pair production as a function of kinematic event variables in pp collisions at  $\sqrt{s} = 7$  and 8 TeV", *Phys. Rev.* **D94** (2016) 052006, doi:10.1103/PhysRevD.94.052006, arXiv:1607.00837.
- [15] CMS Collaboration, "Measurement of differential top-quark pair production cross sections in pp collisions at  $\sqrt{s} = 7$  TeV", *Eur. Phys. J.* **C73** (2013) 2339, doi:10.1140/epjc/s10052-013-2339-4, arXiv:1211.2220.
- [16] CMS Collaboration, "Measurement of differential cross sections for the production of top quark pairs and of additional jets in lepton+jets events from pp collisions at  $\sqrt{s} = 13$  TeV", *Phys. Rev.* **D97** (2018) 112003, doi:10.1103/PhysRevD.97.112003, arXiv:1803.08856.
- [17] ATLAS Collaboration, "Measurements of  $t\bar{t}$  differential cross-sections of highly boosted top quarks decaying to all-hadronic final states in pp collisions at  $\sqrt{s} = 13$  TeV using the ATLAS detector", *Phys. Rev.* **D98** (2018) 012003, doi:10.1103/PhysRevD.98.012003, arXiv:1801.02052.
- [18] ATLAS Collaboration, "Measurement of the differential cross-section of highly boosted top quarks as a function of their transverse momentum in  $\sqrt{s} = 8$  TeV proton-proton collisions using the ATLAS detector", *Phys. Rev.* **D93** (2016) 032009, doi:10.1103/PhysRevD.93.032009, arXiv:1510.03818.

- [781] [19] CMS Collaboration, “Measurement of the integrated and differential  $t\bar{t}$  production cross  
 782 sections for high- $p_t$  top quarks in  $pp$  collisions at  $\sqrt{s} = 8$  TeV”, *Phys. Rev.* **D94** (2016)  
 783 072002, doi:10.1103/PhysRevD.94.072002, arXiv:1605.00116.
- [784] [20] CMS Collaboration, “The CMS experiment at the CERN LHC”, *JINST* **3** (2008) S08004,  
 785 doi:10.1088/1748-0221/3/08/S08004.
- [786] [21] CMS Collaboration, “The CMS trigger system”, *JINST* **12** (2017) P01020,  
 787 doi:10.1088/1748-0221/12/01/P01020, arXiv:1609.02366.
- [788] [22] P. Nason, “A new method for combining NLO QCD with shower Monte Carlo  
 789 algorithms”, *JHEP* **11** (2004) 040, doi:10.1088/1126-6708/2004/11/040,  
 790 arXiv:hep-ph/0409146.
- [791] [23] S. Frixione, P. Nason, and G. Ridolfi, “A Positive-weight next-to-leading-order Monte  
 792 Carlo for heavy flavour hadroproduction”, *JHEP* **09** (2007) 126,  
 793 doi:10.1088/1126-6708/2007/09/126, arXiv:0707.3088.
- [794] [24] S. Frixione, P. Nason, and C. Oleari, “Matching NLO QCD computations with parton  
 795 shower simulations: the POWHEG method”, *JHEP* **11** (2007) 070,  
 796 doi:10.1088/1126-6708/2007/11/070, arXiv:0709.2092.
- [797] [25] S. Alioli, P. Nason, C. Oleari, and E. Re, “A general framework for implementing NLO  
 798 calculations in shower Monte Carlo programs: the POWHEG BOX”, *JHEP* **06** (2010) 043,  
 799 doi:10.1007/JHEP06(2010)043, arXiv:1002.2581.
- [800] [26] S. Alioli, S. O. Moch, and P. Uwer, “Hadronic top-quark pair-production with one jet and  
 801 parton showering”, *JHEP* **01** (2012) 137, doi:10.1007/JHEP01(2012)137,  
 802 arXiv:1110.5251.
- [803] [27] S. Alioli, P. Nason, C. Oleari, and E. Re, “NLO single-top production matched with  
 804 shower in POWHEG: s- and t-channel contributions”, *JHEP* **09** (2009) 111,  
 805 doi:10.1088/1126-6708/2009/09/111, arXiv:0907.4076. [Erratum:  
 806 doi:10.1007/JHEP02(2010)011].
- [807] [28] J. Alwall et al., “The automated computation of tree-level and next-to-leading order  
 808 differential cross sections, and their matching to parton shower simulations”, *JHEP* **07**  
 809 (2014) 079, doi:10.1007/JHEP07(2014)079, arXiv:1405.0301.
- [810] [29] J. Alwall et al., “Comparative study of various algorithms for the merging of parton  
 811 showers and matrix elements in hadronic collisions”, *Eur. Phys. J.* **C53** (2008) 473,  
 812 doi:10.1140/epjc/s10052-007-0490-5, arXiv:0706.2569.
- [813] [30] T. Sjöstrand, S. Mrenna, and P. Z. Skands, “PYTHIA 6.4 physics and manual”, *JHEP* **05**  
 814 (2006) 026, doi:10.1088/1126-6708/2006/05/026, arXiv:hep-ph/0603175.
- [815] [31] T. Sjöstrand, S. Mrenna, and P. Z. Skands, “A brief introduction to PYTHIA 8.1”, *Comput.  
 816 Phys. Commun.* **178** (2008) 852, doi:10.1016/j.cpc.2008.01.036,  
 817 arXiv:0710.3820.
- [818] [32] NNPDF Collaboration, “Parton distributions for the LHC Run II”, *JHEP* **04** (2015) 040,  
 819 doi:10.1007/JHEP04(2015)040, arXiv:1410.8849.

- 820 [33] CMS Collaboration, “Event generator tunes obtained from underlying event and  
821 multiparton scattering measurements”, *Eur. Phys. J.* **C76** (2015) 155,  
822 doi:10.1140/epjc/s10052-016-3988-x, arXiv:1512.00815.
- 823 [34] CMS Collaboration, “Investigations of the impact of the parton shower tuning in Pythia 8  
824 in the modelling of  $t\bar{t}$  at  $\sqrt{s} = 8$  and 13 TeV”, CMS Physics Analysis Summary  
825 CMS-PAS-TOP-16-021, 2016.
- 826 [35] GEANT4 Collaboration, “GEANT4—a simulation toolkit”, *Nucl. Instrum. Meth. A* **506**  
827 (2003) 250, doi:10.1016/S0168-9002(03)01368-8.
- 828 [36] M. Czakon and A. Mitov, “Top++: A program for the calculation of the top-pair  
829 cross-section at hadron colliders”, *Comput. Phys. Commun.* **185** (2014) 2930,  
830 doi:10.1016/j.cpc.2014.06.021, arXiv:1112.5675.
- 831 [37] Y. Li and F. Petriello, “Combining QCD and electroweak corrections to dilepton  
832 production in the framework of the FEWZ simulation code”, *Phys. Rev. D* **86** (2012)  
833 094034, doi:10.1103/PhysRevD.86.094034, arXiv:1208.5967.
- 834 [38] N. Kidonakis, “Top Quark Production”, (2014). arXiv:1311.0283.
- 835 [39] M. Bahr et al., “Herwig++ Physics and Manual”, *Eur. Phys. J.* **C58** (2008) 639,  
836 doi:10.1140/epjc/s10052-008-0798-9, arXiv:0803.0883.
- 837 [40] S. Gieseke, C. Rohr, and A. Siodmok, “Colour reconnections in Herwig++”, *Eur. Phys. J.*  
838 **C72** (2012) 2225, doi:10.1140/epjc/s10052-012-2225-5, arXiv:1206.0041.
- 839 [41] CMS Collaboration, “Particle-flow reconstruction and global event description with the  
840 cms detector”, *JINST* **12** (2017) P10003, doi:10.1088/1748-0221/12/10/P10003,  
841 arXiv:1706.04965.
- 842 [42] M. Cacciari, G. P. Salam, and G. Soyez, “The anti- $k_t$  jet clustering algorithm”, *JHEP* **04**  
843 (2008) 063, doi:10.1088/1126-6708/2008/04/063, arXiv:0802.1189.
- 844 [43] M. Cacciari, G. P. Salam, and G. Soyez, “FastJet user manual”, *Eur. Phys. J.* **C72** (2012)  
845 1896, doi:10.1140/epjc/s10052-012-1896-2, arXiv:1111.6097.
- 846 [44] CMS Collaboration, “Jet energy scale and resolution in the CMS experiment in pp  
847 collisions at 8 TeV”, *JINST* **12** (2017) P02014,  
848 doi:10.1088/1748-0221/12/02/P02014, arXiv:1607.03663.
- 849 [45] J. Thaler and K. Van Tilburg, “Identifying boosted objects with  $N$ -subjettiness”, *JHEP* **03**  
850 (2011) 015, doi:10.1007/JHEP03(2011)015, arXiv:1011.2268.
- 851 [46] S. Catani, Y. L. Dokshitzer, M. H. Seymour, and B. R. Webber, “Longitudinally invariant  
852  $K_t$  clustering algorithms for hadron hadron collisions”, *Nucl. Phys.* **B406** (1993) 187,  
853 doi:10.1016/0550-3213(93)90166-M.
- 854 [47] J. Thaler and K. Van Tilburg, “Maximizing Boosted Top Identification by Minimizing  
855  $N$ -subjettiness”, *JHEP* **02** (2012) 093, doi:10.1007/JHEP02(2012)093,  
856 arXiv:1108.2701.
- 857 [48] M. Dasgupta, A. Fregoso, S. Marzani, and G. P. Salam, “Towards an understanding of jet  
858 substructure”, *JHEP* **09** (2013) 029, doi:10.1007/JHEP09(2013)029,  
859 arXiv:1307.0007.

- 860 [49] J. M. Butterworth, A. R. Davison, M. Rubin, and G. P. Salam, “Jet substructure as a new  
861 Higgs search channel at the LHC”, *Phys. Rev. Lett.* **100** (2008) 242001,  
862 doi:10.1103/PhysRevLett.100.242001, arXiv:0802.2470.
- 863 [50] A. J. Larkoski, S. Marzani, G. Soyez, and J. Thaler, “Soft drop”, *JHEP* **05** (2014) 146,  
864 doi:10.1007/JHEP05(2014)146, arXiv:1402.2657.
- 865 [51] Y. L. Dokshitzer, G. D. Leder, S. Moretti, and B. R. Webber, “Better jet clustering  
866 algorithms”, *JHEP* **08** (1997) 001, doi:10.1088/1126-6708/1997/08/001,  
867 arXiv:hep-ph/9707323.
- 868 [52] M. Wobisch and T. Wengler, “Hadronization corrections to jet cross-sections in deep  
869 inelastic scattering”, in *Proceedings of the Workshop on Monte Carlo Generators for HERA*  
870 *Physics, Hamburg, Germany*, p. 270. 1998. arXiv:hep-ph/9907280.
- 871 [53] CMS Collaboration, “Identification of heavy-flavour jets with the CMS detector in pp  
872 collisions at 13 TeV”, *JINST* **13** (2018) P05011,  
873 doi:10.1088/1748-0221/13/05/P05011, arXiv:1712.07158.
- 874 [54] J. Therhaag, “TMVA Toolkit for multivariate data analysis in ROOT”, *PoS ICHEP2010*  
875 (2010) 510, doi:10.22323/1.120.0510.
- 876 [55] W. Verkerke and D. P. Kirkby, “The RooFit toolkit for data modeling”, *eConf* **C0303241**  
877 (2003) MOLT007, arXiv:physics/0306116.
- 878 [56] ATLAS Collaboration, “Measurement of the Inelastic Proton-Proton Cross Section at  
879  $\sqrt{s} = 13$  TeV with the ATLAS Detector at the LHC”, *Phys. Rev. Lett.* **117** (2016) 182002,  
880 doi:10.1103/PhysRevLett.117.182002, arXiv:1606.02625.
- 881 [57] CMS Collaboration, “CMS Luminosity Measurements for the 2016 Data Taking Period”,  
882 CMS Physics Analysis Summary CMS-PAS-LUM-17-001, 2017.
- 883 [58] P. Skands, S. Carrazza, and J. Rojo, “Tuning PYTHIA 8.1: the Monash 2013 tune”, *Eur.  
884 Phys. J.* **C74** (2014) 3024, doi:10.1140/epjc/s10052-014-3024-y,  
885 arXiv:1404.5630.
- 886 [59] S. Schmitt, “TUnfold: an algorithm for correcting migration effects in high energy  
887 physics”, *JINST* **7** (2012) T10003, doi:10.1088/1748-0221/7/10/T10003,  
888 arXiv:1205.6201.